

# Stochastic modeling of surface scalar-flux fluctuations in turbulent channel flow using one-dimensional turbulence

Marten Klein<sup>a,\*</sup>, Heiko Schmidt<sup>a</sup>, David O. Lignell<sup>b</sup>

<sup>a</sup>*Lehrstuhl Numerische Strömungs- und Gasdynamik, Brandenburgische Technische Universität Cottbus-Senftenberg, Siemens-Halske-Ring 15A, 03046 Cottbus, Germany*

<sup>b</sup>*Chemical Engineering, CB 350, Brigham Young University, Provo, UT 84602, USA*

---

## Abstract

Accurate and economical modeling of near-surface transport processes is a standing challenge for various engineering and atmospheric boundary-layer flows. In this paper, we address this challenge by utilizing an economical stochastic one-dimensional turbulence (ODT) model. ODT aims to resolve all relevant scales of a turbulent flow for a one-dimensional domain. Here ODT is applied to turbulent channel flow as stand-alone tool. The ODT domain is a wall-normal line that is aligned with the mean shear. The free model parameters are calibrated once for the turbulent velocity boundary layer at a fixed Reynolds number. After that, we use ODT to investigate the Schmidt ( $Sc$ ) and Reynolds ( $Re$ ) number dependence of the scalar boundary-layer structure, turbulent fluctuations, transient surface fluxes, mixing, and transfer to a wall. We demonstrate that the model is able to resolve relevant wall-normal transport processes across the turbulent boundary layer and that it captures state-space statistics of the surface scalar-flux fluctuations. In addition, we show that the predicted mean scalar transfer, which is quantified by the Sherwood ( $Sh$ ) number, self-consistently reproduces established scaling regimes and asymptotic relations. For high asymptotic  $Sc$  and  $Re$ , ODT results fall between the Dittus–Boelter,  $Sh \sim Re^{4/5} Sc^{2/5}$ , and

---

\*Corresponding author. Tel.: +49-(0)355-695-127; Fax: +49-(0)355-694-891.

Email addresses: [marten.klein@b-tu.de](mailto:marten.klein@b-tu.de) (Marten Klein), [heiko.schmidt@b-tu.de](mailto:heiko.schmidt@b-tu.de) (Heiko Schmidt), [davidlignell@byu.edu](mailto:davidlignell@byu.edu) (David O. Lignell)

Colburn,  $Sh \sim Re^{4/5} Sc^{1/3}$ , scalings but they are closer to the former. For finite  $Sc$  and  $Re$ , the model prediction reproduces the relation proposed by Schwertfirm and Manhart (*Int. J. Heat Fluid Flow*, **28**, 1204–1214, 2007) that is based on boundary-layer theory and yields a locally steeper effective scaling than any of the established asymptotic relations. The model extrapolates the scalar transfer to small asymptotic  $Sc \ll Re_\tau^{-1}$  (diffusive limit) with a functional form that has not been previously described.

*Keywords:* one-dimensional turbulence, passive scalar, scalar transfer, surface heat and momentum flux, Reynolds and Schmidt number dependence

*2010 MSC:* 76F25, 76F25, 80A20, 82C31, 82C70

---

## 1. Introduction

Numerical modeling of scalar transport in turbulent boundary layers is a standing challenge that is relevant for a wide range of applications from, small flames to large atmospheric flows. Key problems are related to small-scale correlations, scale interactions, and counter-gradient fluxes (e.g. [1–3]). Due to the latter, all relevant scales of the flow have to be resolved for robust numerical predictions. Direct numerical simulation (DNS) is the ideal tool, but it is of limited applicability due to the resolution requirements imposed by the Kolmogorov and Batchelor scales (e.g. [4–6]). Therefore, the development of feasible but physically accurate fluctuation resolving flow and transport models has been identified as a key challenge (e.g. [7–9]). Here we address the numerical challenge of fluctuation modeling by utilizing an economical stochastic one-dimensional turbulence (ODT) model [10, 11].

ODT has been validated from a fundamental point of view and applied to multi-physics boundary layers (e.g. [12–15]). In such applications, ODT aims to provide full resolution of the whole range of relevant scales with modeling in the physical coordinate. Based on the capturing of the momentum boundary layer [10], it has been assumed that ODT ‘automatically’ captures also scalar transport processes with similar fidelity, with ensuing applications, but this was never

20 systematically investigated. In this paper, we extend two preliminary studies  
[16, 17] and test the assumption mentioned and discuss also the limitations of  
the simple model so that it can be more confidently applied. This is specifically  
important as ODT is used for model development and simulation, for instance,  
as subgrid model in large-eddy simulation [18–20], among other uses.

25 Here we apply the model to canonical channel flow configurations with height  
 $h = 2\delta$ , as sketched in figure 1, and investigate the Schmidt and Reynolds  
number dependence of the bulk-surface coupling in terms of the scalar transfer to  
the wall by distinguishing molecular (diffusive) and turbulent (advective) wall-  
normal transport processes. ODT facilitates the analysis of fluctuating surface  
30 scalar and momentum fluxes and their relation to low-order flow statistics in  
the turbulent boundary layer. For the analysis of scalar transport, we focus  
on a passive scalar that is given by weak temperature variations or a chemical  
tracer that has negligible effect on the mass, momentum, and energy balances  
[21]. Most of the results shown below have been obtained for constant scalar  
35 value (CSV) wall-boundary conditions (that is, isothermal walls), but we also  
consider the complementary case of a prescribed constant scalar flux (CSF; that  
is, a heated channel).

This paper is organized as follows. The ODT model is formulated in sec-  
tion 2. We then summarize the model application and calibration for channel  
40 flow in section 3. In section 4, we report and discuss model predictions for pas-  
sive scalar turbulence statistics in the boundary layer and their relation to the  
state-space of surface flux fluctuations as well as the mean scalar transfer to a  
wall. Section 5 concludes the paper, and some additional material is presented  
in the appendix.

## 45 **2. Model formulation**

Kerstein’s [10, 11] one-dimensional turbulence model aims to resolve all rel-  
evant scales of a turbulent flow. This is made feasible for high Schmidt and  
Reynolds number flows by modeling the effects of turbulent eddies by a stochas-

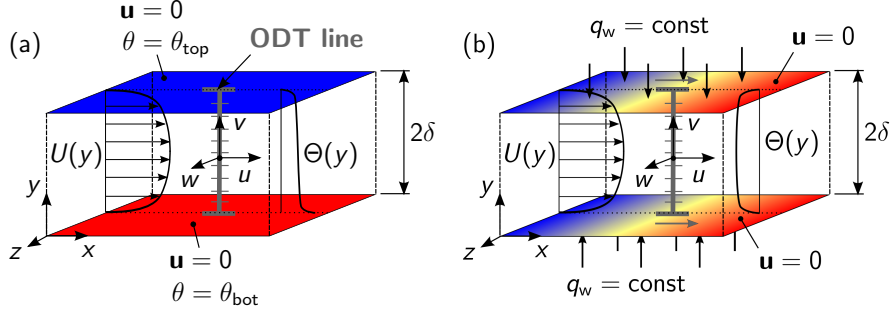


Figure 1: Schematic of the channel flow configuration and the scalar forcing mechanisms investigated. ODT simulations are carried out for a lower-order computational domain, the so-called ‘ODT line’, that spans the whole channel of height  $h = 2\delta$ . (a) Constant scalar value (CSV) forcing with fixed wall values  $\theta_{\text{bot}} \neq \theta_{\text{top}}$ . (b) Constant scalar flux (CSF) forcing with prescribed isoflux wall-boundary condition for which an ODT line nominally moves downstream with the bulk velocity during a simulation.

tic process. The model directly resolves molecular-diffusive transport processes  
 50 and distinguishes them from turbulent-advective transport processes for a lower-  
 order computational domain, termed the ‘ODT line’ in figure 1. Hence, there  
 is no subgrid closure and no closure modeling involved in the present ODT ap-  
 plication. In the following, we give a brief but complete model description for  
 to aid the discussion of the results.

### 55 2.1. Governing equations and physical control parameters

Here we limit our attention to constant-density flows with a passive scalar  
 that has the same mass density as the surrounding fluid. The lower-order  
 stochastic equations may be written as

$$\frac{\partial \mathbf{u}}{\partial t} + \mathcal{E}_{\mathbf{u}}(\alpha) = \nu \frac{\partial^2 \mathbf{u}}{\partial y^2} - \frac{1}{\rho} \frac{dP}{dx} \mathbf{e}_x, \quad \frac{\partial \theta}{\partial t} + \mathcal{E}_{\theta} = \Gamma \frac{\partial^2 \theta}{\partial y^2} + s_{\theta}, \quad (1a, b)$$

where  $\mathbf{u} = (u, v, w)^{\text{T}}$  denotes the velocity vector and its Cartesian components,  
 $\theta$  the scalar,  $t$  the time,  $x$  the stream-wise and  $y$  the vertical coordinate,  $\rho$  and  
 $\nu$  the fluid’s density and kinematic viscosity,  $\Gamma$  the scalar diffusivity,  $dP/dx$  the  
 prescribed mean pressure gradient,  $\mathbf{e}_x$  the unit vector in stream-wise direction,

60  $s_\theta$  is a scalar source term, and  $\mathcal{E}$  represents the stochastic eddy events.  $\mathcal{E}_u(\alpha)$  and  $\mathcal{E}_\theta$  are coupled but described in more detail below.

A suitable nondimensional form of the governing equations (1a,b) may be obtained with the aid of the mean wall-stress balance and the friction scalar property (temperature or concentration),

$$u_\tau^2 = \nu \left| \frac{dU}{dy} \right|_w = \frac{\delta}{\rho} \left| \frac{dP}{dx} \right|, \quad \theta_\tau = \frac{\Gamma}{u_\tau} \left| \frac{d\Theta}{dy} \right|_w, \quad (2a, b)$$

where the upper-case symbols  $U(y) = \overline{u(y,t)}$  and  $\Theta(y) = \overline{\theta(y,t)}$ , as well as the bar,  $\overline{(\cdot)}$ , denote conventional temporal (Reynolds) averages,  $u_\tau$  and  $\theta_\tau$  are the friction velocity and scalar property, respectively, and the subscript ‘w’ indicates evaluation at the wall. Scaling equations (1a,b) with the friction variables yields

$$\frac{\partial \mathbf{u}^+}{\partial t^+} + \mathcal{E}_u^+(\alpha) = \frac{1}{Re_\tau} \frac{\partial^2 \mathbf{u}^+}{\partial y^{+2}} + \mathbf{e}_x, \quad \frac{\partial \theta^+}{\partial t^+} + \mathcal{E}_\theta^+ = \frac{1}{Sc Re_\tau} \frac{\partial^2 \theta^+}{\partial y^{+2}} + s_\theta^+, \quad (3a, b)$$

where  $y^+ = yu_\tau/\nu$ ,  $t^+ = tu_\tau/\delta$ ,  $u^+ = u/u_\tau$ , and  $\theta^+ = (\theta - \theta_w)/\theta_\tau$  denote variables in inner scaling and  $\theta_w$  is a reference (wall) value of the scalar property. Similarity solutions are obtained with dependence on the friction Reynolds, 65  $Re_\tau = \delta u_\tau/\nu$ , and Schmidt (Prandtl),  $Sc = \nu/\Gamma$ , numbers.

No-slip wall-boundary conditions are prescribed for the velocity vector, whereas fixed-value and isoflux boundary conditions are prescribed for the scalar, respectively. The boundary conditions for the scalar define the case set-up, which is addressed in more detail in Appendix A.

## 70 2.2. Discrete eddy events and map-based advection modeling

Discrete eddy events are used to formulate the stochastic terms in equations (1a,b). This involves two mathematical operations to represent the effects of turbulent advection and pressure fluctuations. When an eddy event is selected, the variables at location  $f(y)$  are instantaneously replaced by the values at mapped location  $y$ . For the scalar and the velocity vector, these opera-

tions [11] are given by

$$\mathcal{E}_\theta : \theta(y) \rightarrow \theta''(y) = \theta(f(y)) , \quad \mathcal{E}_\mathbf{u}(\alpha) : \mathbf{u}(y) \rightarrow \mathbf{u}''(y) = \mathbf{u}(f(y)) + \mathbf{c}(\alpha) K(y) , \quad (4a, b)$$

where  $f(y)$  denotes a mapping function,  $K(y) = y - f(y)$  a kernel function, and  $\mathbf{c} = (c_1, c_2, c_3)^T$  the coefficients that are used to model the effect of pressure fluctuations. These coefficients control the redistribution of the kinetic energy among the velocity components.

75 In Navier–Stokes turbulence, the turnover of a single eddy locally increases the gradients of the flow variables on the length scale of that eddy. This process is addressed in ODT by the triplet map [10]. For an eddy event of size  $l$  occurring at location  $y_0$ , the triplet map affects the interval  $[y_0, y_0 + l]$ ; this is given by

$$f(y) = y_0 + \begin{cases} 3(y - y_0) & \text{for } y - y_0 \in [0, l/3] , \\ 2l - 3(y - y_0) & \text{for } y - y_0 \in [l/3, 2l/3] , \\ 3(y - y_0) - 2l & \text{for } y - y_0 \in [2l/3, l] , \\ y - y_0 & \text{otherwise.} \end{cases} \quad (5)$$

In the dynamically adaptive grid implementation of the ODT model used  
80 here, profiles of the flow variables are spatially compressed by a factor of three, then the copies are sequentially arranged to fill the eddy size interval with the central copy spatially reversed in order to ensure continuity [25]. Irrespective of the implementation details, the important properties of the triplet map are that it is (i) measure-preserving, and (ii) does not introduce discontinuities along the  
85 ODT line. These two aspects are important for the conservation properties of the method. Note that, due to the triplet map, kinetic energy is brought from large to small scales in a scale-local fashion, which is consistent with the behavior of the turbulent energy cascade.

Next, we continue with modeling of pressure-velocity couplings in the mo-  
90 mentum equation. The last term in equation (4b) models the effect of a fluctuating pressure gradient. The kernel function  $K(y)$  is a measure for the map-induced fluid displacement and the coefficient vector  $c_i$  scales the efficiency of the inter-component kinetic energy transfer.

The change of the kinetic energy in the  $i^{\text{th}}$  velocity component due to the  
 95 application of an eddy event, as expressed by equation (4b), is given by

$$\Delta E_i = \frac{1}{2l} \int_{y_0}^{y_0+l} [u_i''^2(y) - u_i^2(y)] dy. \quad (6)$$

Energy conservation requires that the sum of the changes vanishes:  $\Delta E_1 + \Delta E_2 + \Delta E_3 = 0$  [11]. The  $c_i$  are obtained by a maximization of the inter-component kinetic energy transfer (that is,  $-\Delta E_i$ ) with respect to  $c_i$ . This yields

$$c_i = \frac{1}{K_K} \left[ -u_{K,i} + \text{sgn}(u_{K,i}) \sqrt{(1-\alpha)u_{K,i}^2 + \frac{\alpha}{2}(u_{K,j}^2 + u_{K,k}^2)} \right], \quad (7)$$

where  $u_{K,i} = \int u_i(f(y)) K(y) dy$  denotes the kernel-weighted components of the  
 100 velocity vector,  $K_K = \int K^2(y) dy$  the squared kernel, which is related to the map-induced fluid displacement, the indexes  $(ijk)$  are permutations of  $(123)$ , and  $\alpha$  is a model parameter that controls the efficiency of the inter-component energy transfer due to fluctuating pressure gradient forces. The parameter  $\alpha$  specifies the fraction of the available (extractable) kinetic energy that is actually  
 105 used for redistribution [11]. It takes values between 0 (no redistribution) and 1 (maximal redistribution).  $\alpha = 2/3$  corresponds to an equal partitioning of energy among velocity components, that is, a relaxation to locally homogeneous isotropic turbulence [11], and is commonly applied in ODT simulations. Here we select  $\alpha = 1/6$  from a calibration of near-surface velocity fluctuations that  
 110 are addressed in sections 3 and 4.3.

### 2.3. Stochastic selection of eddy events

Eddy events are characterized by three random variables: the eddy size  $l$ , the position  $y_0$ , and the time  $t$  of occurrence. In theory, these variables can be sampled from an eddy-rate distribution  $\lambda$ , whereby  $\lambda(l, y_0, t) dl dy_0 dt$  gives the  
 115 number of eddy events in the size range  $[l, l+dl]$ , the position range  $[y_0, y_0+dy_0]$  and the time interval  $[t, t+dt]$ . This distribution is expensive to compute, and depends on the evolving flow state, further complicating its construction and sampling.

In practice, eddies are sampled from the  $\lambda$  distribution using the efficient  
120 thinning-and-rejection method [10]. For this purpose, the eddy-rate distribution  
is written using dimensional arguments. With  $l$  as an eddy length scale, we have  
 $\lambda = C \tau^{-1} l^{-2}$ , where  $C$  is a proportionality constant (model parameter) that  
scales the eddy rate, and  $\tau$  is the eddy time scale (eddy turnover time). This  
time scale written in terms of the total extractable (shear-available) kinetic  
125 energy per unit mass, which, for the instantaneous velocity components  $u_i(y, t)$   
and a selected eddy event of size  $l$ , is given by

$$\frac{l^2}{\tau^2} \sim \frac{1}{l^4} \sum_{i=1}^3 u_{K,i}^2 - Z \frac{\nu^2}{l^2}. \quad (8)$$

Here, it follows from the construction that the kernel-weighted velocities can be  
summed instead of the kinetic energies. This shows that the total extractable  
kinetic energy does not depend on the inter-component energy transfer, or the  
130 model parameter  $\alpha$ . The last term in equation (8) is included to model the  
damping effects of the viscosity. The model parameter  $Z > 0$  is used to suppress  
unphysically small eddy events through an energetic penalty condition [10].  
Values  $Z \gg 1$  have been suggested for wall-bounded flows [10, 18] to make  
the model aware of the viscous sublayer by suppressing wall-attached eddies  
135 below the critical local Reynolds number  $Re_c = u_e l / \nu = \sqrt{Z}$ , where  $u_e =$   
 $(u_K^2 + v_K^2 + w_K^2)^{1/2}$ .

Finally, the eddy time scale  $\tau$  can be computed from the instantaneous  
velocity vector components  $u_i(y, t)$  once the location  $y_0$  and size  $l$  of an eddy  
event have been selected,

$$\frac{1}{\tau} = \sqrt{\frac{1}{l^6} (u_K^2 + v_K^2 + w_K^2) - Z \frac{\nu^2}{l^4}}. \quad (9)$$

140 This time scale is compared with the mean sampling time scale,  $\tau_s$ , to obtain the  
acceptance probability  $p_a = \tau_s / \tau \ll 1$  of a physically plausible eddy event. The  
point in time at which equation (9) is evaluated is obtained with the aid of a  
marked Poisson process. This process assumes that eddy events are independent  
of each other so that the time increment between two such events can be sampled  
145 economically from an exponential distribution with the mean rate  $\tau_s^{-1}$  [10].

The eddy location  $y_0$  and size  $l$  that are used to compute the corresponding time scale  $\tau$  are sampled from a uniform distribution on the domain and model distribution, respectively. These distributions affect the efficiency of the sampling algorithm, but not the accuracy of the sampled eddy distribution by construction of the thinning-and-rejection method; see [26] and references  
150 therein for details.

It is sometimes important to suppress unphysically large eddy events, which may occur rarely in the sampling procedure but have significant effect on the mixing process. A simple suppression mechanism is often sufficient for confined  
155 flows. For fully-developed channel flow, turbulence statistics must be symmetric about the channel center. Based on Prandtl's mixing length theory [27] and the attached eddy model [28, 29], it has been suggested [18] to constrain the maximum eddy size by the channel half height, that is,  $l_{\max} = \delta$ , which is done here.

#### 160 2.4. Remarks on the numerical solver implementation

The stochastic terms denoted by  $\mathcal{E}$  above are zero in between any two instantaneous eddy events so that a set of one-dimensional diffusion equations is solved continuously in time until the next eddy event occurs. The time advancement is done here with the explicit Euler method. The implicit Euler method  
165 has been used for a couple of cases, though with little effect on the simulation efficiency that is limited by the eddy sampling procedure. Higher order methods are implemented, but the instantaneous implementation of the stochastic mapping events nevertheless results in a first-order global scheme.

Spatial discretization along the ODT domain is done with a Lagrangian  
170 finite-volume method on an adaptive grid [25]. The velocity vector and the passive scalar are located at the cell centers. The minimum allowed cell size,  $\Delta y_{\min}$ , which is needed for dynamic re-meshing, is of the order of the Batchelor scale that can be estimated as  $\eta_B/\delta \simeq Sc^{-1/2} Re^{-3/4}$ , where  $Re$  denotes the bulk Reynolds number, which can be estimated for fully-developed turbulent  
175 channel flow by inverting  $Re_\tau = 0.18 Re^{0.88}$  [30]. The maximum allowed cell

size is set to  $\Delta y_{\max} \simeq 20 \Delta y_{\min}$  in order to minimize any numerical transport.

In the adaptive mesh ODT formulation [25], the grid density increases in eddy regions during eddy events, consistent with the factor-of-three spatial compression of the triplet maps. This eddy region undergoes mesh adaption again at the end of the diffusive advancement process, and the local (versus domain-  
180 global) adaption is done to minimize numerical effects of the meshing operations. However, a given region is subject to mesh adaption if it has not had an eddy event and been adapted within some multiple ( $\beta_{\text{DA}}$ ) of the diffusion time scale, where  $\beta_{\text{DA}} \simeq 10$  is used.

### 185 **3. Model application and calibration**

In this section we address the general model application to channel flow and some fundamental properties of the stochastic model for the velocity boundary layer. We do this in order to calibrate the free model parameters and in order to quantify the model’s ability to capture turbulent fluctuations.

#### 190 *3.1. ODT simulation of turbulent channel flow*

ODT simulations of turbulent channel flows are conducted as follows. Equations (1a,b) are numerically integrated which yields a time sequence of synthetic but statistically representative flow profiles. Conventional statistics are performed on these profiles and gathered on a predefined post-processing grid for the fully-adaptive solver [25] used. While cumulative statistics are straightforward, the computation of the ODT-resolved turbulent fluxes (cross-correlations)  
195 is conditional on the eddy events and detailed in Appendix B.

We have performed ‘pre-simulations’ for isothermal flow conditions at various  $Re_\tau$  in order to calibrate the free model parameters  $C$ ,  $Z$ , and  $\alpha$ . The individual influence of these parameters on the velocity boundary-layer statistics is discussed, for example, in [18, 31] and not repeated here. We select  $C = 6$ ,  
200  $Z = 300$ , and  $\alpha = 1/6$  as reasonable model parameter values for the presently investigated  $Re_\tau$  range. The calibrated model parameters are kept fixed from

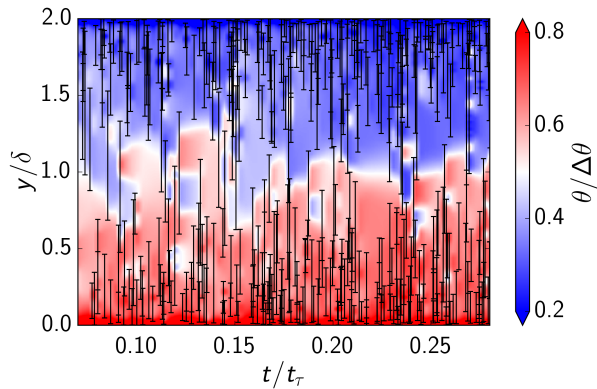


Figure 2: Space-time diagram of ODT eddy events (black lines) together with a  $Sc = 3$  passive scalar (color shading) in a channel flow with  $Re_\tau = 180$ . The scalar is prescribed by fixed wall values (CSV forcing) and perturbed on multiple scales by the stochastically sampled and instantaneously implemented eddy events in between which only molecular diffusion occurs.

here on. We comment on relevant aspects of the model parameter selection  
 205 below.

At this point we briefly describe how the stochastic (turbulent advective) and deterministic (molecular diffusive) transport processes interact. Figure 2 shows a space-time diagram of an ODT solution of a turbulent channel flow with  $Re_\tau = 180$  and  $Sc = 3$ . The scalar is prescribed by fixed wall values that  
 210 differ by  $\Delta\theta = \theta_{\text{bot}} - \theta_{\text{top}} > 0$ . The scalar field fluctuates notably in the bulk due to application of the triplet maps. The mapping intervals form a random sequence and are given as black vertical lines. Intense turbulent mixing occurs where lines of different size cluster. Note that eddy events are mostly ‘anchored’ in the near-surface region for turbulent channel flow, which is the ODT analog  
 215 of the attached-eddy model (e.g. [28, 29]). Note that it is a dynamical feature of the ODT formulation that captures these physical properties qualitatively.

ODT simulations need to sufficiently sample the state space. We therefore ran long-time simulations with  $t_a u_\tau / \nu \gg 1$ , where  $t_a$  is the simulated averaging time interval per realization and  $\delta / u_\tau$  a statistical eddy turnover time. If nec-  
 220 essary,  $t_a$  can be significantly reduced by adopting large  $M$  ensembles of flow

realizations. The numerical solver used is fully adaptive such that the stochastic ODT simulations performed were *permissively* resolving a boundary-layer diffusive length scale that is the Kolmogorov or Batchelor scale of the wall-bounded flow for  $Sc \leq 1$  and  $Sc > 1$ , respectively. The minimum grid cell size is  $\Delta y_{\min}$  and is assured to be smaller than the estimated Kolmogorov and Batchelor scales. Table 1 summarizes relevant details and bulk quantities for a representative set of ODT simulations.

### 3.2. Model calibration for the velocity boundary layer

We now aim to evaluate the general model fidelity in terms of low-order velocity statistics in the turbulent boundary layer for the calibrated model parameters by comparison with available reference data. Figure 3(a) shows normalized mean velocity profiles,  $U^+ = U/u_\tau$ , for various  $Re_\tau$  for the calibrated model. Simulated mean velocity profiles are consistent with the empirical law-of-the-wall of high asymptotic  $Re_\tau$  [32]. This demonstrates the model consistency and convergence for highly turbulent flows with large Reynolds number. The ODT model accurately captures not only the log layer, but also the linear (viscous) layer right at the wall. However, it does not fully capture the buffer and outer layers of the reference DNS [33, 34].

Figure 3(b) shows the normalized Reynolds stress component  $\overline{u'^+v'^+}$ , which is in very good agreement with the reference DNS [33, 34]. This implies model consistency in the log and linear layers with the mean velocity and mean shear including wall-normal stresses.

Figures 3(c) and 3(d) show the normalized root-mean-square (rms) fluctuation velocity components,  $u'_{\text{rms}}^+ = (\overline{u'^2} - U^2)^{1/2}/u_\tau$  and  $v'_{\text{rms}}^+ = (\overline{v'^2})^{1/2}/u_\tau$ , respectively, as vertical ‘back-to-back’ plots with reference DNS data [33] mirrored at the horizontal axis (negative fluctuation velocity) for visibility. In ODT, the fluctuation velocities are generally underestimated, which is a known modeling artifact (e.g. [10, 11, 18, 31]). The location of the inner (near-wall) peak of  $u'_{\text{rms}}^+$  is captured but the peak itself is degraded due to the micro-structure modeling in the discrete eddy events [25]. The outer peak in  $u'_{\text{rms}}^+$  that emerges

Table 1: Details of ODT simulation parameters and bulk quantities for representative cases with two different scalar wall-boundary conditions ( $\theta$ -BC).  $Re_\tau$  and  $Re$  denote the bulk friction Reynolds number, respectively,  $Sc$  the Schmidt number,  $K^+ = \theta_\tau/\Delta\theta$  the scalar transfer coefficient where  $\Delta\theta = |\overline{(\theta_b - \theta_w)}|$  is the mean scalar bulk-wall difference,  $\bar{N}_y$  the average number of cells in the adaptive grid,  $\Delta y_{\min}^+$  the minimum allowed cell size, and  $t_s u_\tau/\delta$  the simulated eddy turnover times per realization. Core hours (CPU-h) spent per realization measured on Intel® Xeon® E5-2630 (2.40 GHz) processors.

$Re_\tau$	$Re$	$Sc$	$K^+$	$\theta$ -BC	$\bar{N}_y$	$\Delta y_{\min}^+$	$t_s u_\tau/\delta$	CPU-h
180.4	2660	0.025	0.275	CSV	166	0.2	15,000	5.5
180.4	2663	0.71	0.0475	CSV	163	0.2	15,000	5.5
180.2	2665	10	0.0150	CSV	164	0.2	15,000	7.5
180.0	2716	200	0.00251	CSV	170	0.036	1500	20
180.0	2723	1000	0.000893	CSV	174	0.018	1500	68
591.5	10,806	0.025	0.130	CSV	207	0.12	4500	5.5
591.5	10,809	0.71	0.0426	CSV	203	0.12	4500	5.5
590.3	10,890	10	0.0147	CSV	198	0.12	4500	7.5
590.0	11,216	200	0.00255	CSV	207	0.024	450	25
589.4	11,360	1000	0.000907	CSV	218	0.012	450	97
994.2	19,126	0.025	0.164	CSF	223	0.36	2000	94
994.5	19,133	0.71	0.0523	CSF	225	0.36	2000	94
2007	43,552	0.025	0.0827	CSV	273	0.4	1200	93
2008	43,607	0.71	0.0381	CSV	285	0.4	1200	94
2007	43,599	10	0.0139	CSV	269	0.4	1200	56
1993	44,563	200	0.00243	CSV	871	0.08	300	33
2017	43,237	1000	0.000862	CSV	1195	0.08	300	38
5222	125,750	0.025	0.0655	CSV	526	0.21	480	31
5223	125,874	0.71	0.0351	CSV	551	0.21	480	31
5213	126,803	10	0.0139	CSV	2737	0.1	480	19
5271	125,370	200	0.00252	CSV	3256	0.1	240	64
5269	125,411	1000	0.000904	CSV	7144	0.1	120	33

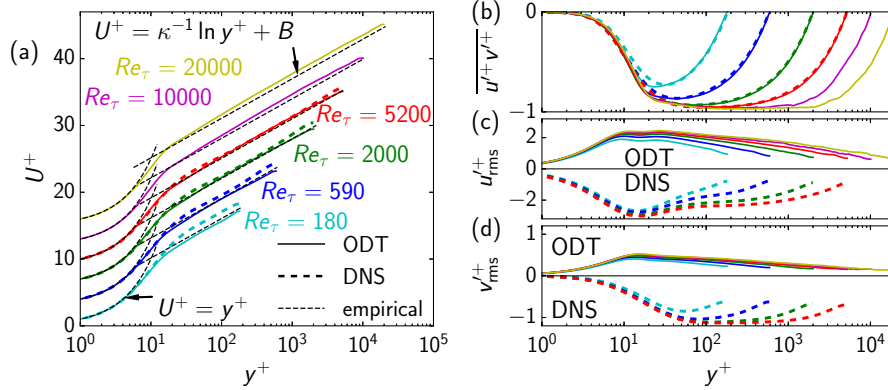


Figure 3: (a) Mean stream-wise velocity,  $U^+$  (offset by  $\Delta U^+ = 3$  for visibility), (b) wall-normal momentum flux,  $\overline{u'+v'+}$ , (c) stream-wise,  $u'_{\text{rms}}$ , and (d) wall-normal,  $v'_{\text{rms}}$ , root-mean-square (rms) fluctuation velocity components for various  $Re_\tau$ . Panels (c) and (d) are vertical ‘back-to-back’ plots with reference data (negative values, dashed) mirrored at the  $y^+$  axis for better visibility. Reference DNS results are from [33, 34]. The empirical law-of-the-wall is given for high asymptotic Reynolds numbers yielding the log-layer parameterization coefficients  $\kappa = 0.389$  and  $B = 4.23$  [32].

at high  $Re_\tau$  is only marginally captured by the model [31].

The wall-normal fluctuation variance,  $v'_{\text{rms}}^+$ , which is shown in figure 3(d), is generally less well captured than  $u'_{\text{rms}}^+$ , except for the surface layer region with  $y^+ < 5$  for the model setup used. The latter aspect is crucial with respect to capturing transient surface fluxes which is the primary motivation for this study that focuses on wall-normal transport and models stream- and span-wise contributions in the same way by a simple kernel mechanism that is given in equation (4b). Note that eddy turbulent advection in ODT is performed by the triplet map (5) such that  $v'$  is *not* a turbulent advecting velocity. Instead, the fluctuation variance  $\overline{v'^2}$  (and, hence, also  $v'_{\text{rms}}^+$ ) is a measure for the contribution from the  $v$  velocity component to the model-resolved eddy turbulent kinetic energy. It is therefore less surprising that the turbulent flux  $\overline{u'v'}$  is well captured by the map-based advection even though  $u'$  and  $v'$  (as well as  $w'$ ) are not fully captured by the model [18].

Next, we analyze the turbulent kinetic energy (TKE) in order to quantify the

model-resolved fluctuating momentum transport across the velocity boundary layer. The TKE budget balance is given by (see e.g. [30])

$$\frac{\partial k}{\partial t} + \mathbf{U} \cdot \nabla k = P + \varepsilon + D + T, \quad (10)$$

where  $k = \overline{u'_i u'_i} / 2$  denotes the TKE,  $P$  the turbulent production,  $\varepsilon$  the dissipation,  $D$  the diffusive transport, and  $T$  the turbulent transport of the TKE. The left-hand side vanishes for statistically stationary channel flow, and the terms on the right-hand side only retain their wall-normal contributions within the ODT modeling framework. Following [10], we obtain the following model-resolved terms:

$$P = -\overline{v' u'} \frac{dU}{dy}, \quad \varepsilon = -\nu \overline{\frac{\partial u'_i}{\partial y} \frac{\partial u'_i}{\partial y}}, \quad D = \nu \frac{d^2 k}{dy^2}, \quad T = -\frac{d \overline{v' u'_i u'_i}}{dy}. \quad (11a, b, c, d)$$

265 The corresponding nondimensional expressions for these terms are obtained by division with  $u_\tau^4 / \nu$ , which is indicated by the super-script ‘+’. Note that the fluctuating pressure transport is not directly resolved by ODT. However, pressure transport is implicitly modeled in the fluctuating terms that are stochastically modeled. Note further that we compute cross-correlations, like  $\overline{u'v'}$ , directly but  
 270 diagnostically from conditional eddy event statistics. The procedure is described in Appendix B below.

Figure 4 shows the TKE budget balance for the model-resolved terms together with reference data. One can see that all terms are qualitatively captured. There is good quantitative agreement for the production, but the dissipation and  
 275 transport terms agree quantitatively only towards the bulk. Hence, the momentum transport across the buffer layer,  $5 < y^+ < 30$ , is somewhat different in the lower-order stochastic representation of the turbulent dynamics. Nevertheless, we emphasize that the model is consistent in exhibiting a balance of the resolved budget terms (dotted line).

#### 280 4. Results and discussion

In the following, we investigate the scalar boundary layer, fluctuations and wall-normal fluxes using conventional statistics. We then turn to the detailed

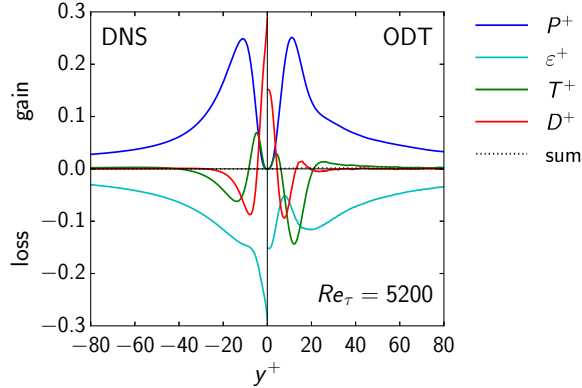


Figure 4: ‘Back-to-back’ plot of the turbulent kinetic energy (TKE) budget balance for  $Re_\tau = 5200$  showing ODT results for  $y^+ \geq 0$  and corresponding DNS from [33] for  $y^+ \leq 0$ .

statistics of the transient surface scalar and momentum fluxes which govern the fluid-surface coupling but are commonly not resolved in filter-based approaches  
 285 such as LES and RANS. Next, the modeled scalar fluctuation variance and mixing properties are investigated for wall-bounded turbulence. Finally, we address ODT’s capabilities for extrapolation by investigating the scaling regimes of the mean surface scalar transfer. This is done with the calibrated model set-up and primarily for fixed-value (CSV) forcing of the scalar. Isoflux (CSF) forcing  
 290 is used to demonstrate boundary layer similarity and for direct comparisons with available reference data.

#### 4.1. Scalar boundary layer

Recently, evidence from DNS was presented that the dissimilarity of scalar and momentum transport manifests itself also in the boundary layer structure  
 295 [4, 35] which has been long known from measurements (e.g. [36]). DNS resolve the intricate dynamics in the turbulent boundary layer and have thus been the tool of choice (e.g. [2, 24, 37]). The question addressed in the following, therefore, is to what extent the lower-order ODT model is able to capture the scalar boundary layer structure?

300 Wall-normal profiles of the normalized scalar mean field,  $\Theta^+ = (\bar{\theta} - \theta_w)/\theta_\tau$ , are shown for various  $Re_\tau$  in figure 5(a) and 5(b) for  $Sc \leq 0.71$  and  $Sc \geq 0.71$ ,

respectively, where  $y^+$  serves as boundary-layer coordinate. In figure 5(a), a linear sublayer can be discerned for  $y^+ < 10$  where all data collapse on the diffusive reference curve  $\Theta^+ = Sc y^+$  (thin dashed). The sublayer extends up to  $y^+ \approx 200$  for the more diffusive cases with  $Sc = 0.025$ . Hence, a log layer can only be discerned for high enough  $Re_\tau$ , that is, for friction Peclet number  $Pe_\tau = Re_\tau Sc \geq O(100)$  such that the scalar boundary layer extends beyond  $y^+ \simeq O(100)$ . The log region is indicated by empirical fits (oblique black dashed lines) to the ODT results with  $Re_\tau = 20,000$  for the range  $80 < y^+ < Re_\tau/2$ . The functional dependence is given by

$$\Theta^+ = \kappa_\theta^{-1} \ln y^+ + B_\theta, \quad (12)$$

where  $\kappa_\theta$  is the scalar von Kármán ‘constant’ and  $B_\theta$  the scalar additive ‘constant’ that may retain a dependence on  $Sc$  and  $Re_\tau$  [2, 38]. The fitted values of  $\kappa_\theta$  and  $B_\theta$  are shown in figures 5(c) and figures 5(d, e), respectively, for all ODT simulations conducted in this study and to be discussed below in more detail. The boundary layer structure obtained with ODT is consistent with available reference DNS [1, 2, 39] for  $Sc = 0.7$  and 0.025, respectively. In these DNS, the scalar is either prescribed by CSF ( $\Theta^+$  bending downward for large  $y^+$ ) or CSV ( $\Theta^+$  bending upward) such that the functional dependence  $\Theta^+(y^+)$  takes a different form in the outer layer depending on the scalar forcing [2], which is fully captured by ODT.

For cases with  $Sc \geq 10$  shown in figure 5(b), the ODT boundary-layer structure is in reasonable agreement with available reference DNS [4, 5]. Without loss of generality for the boundary layer structure, these high  $Sc$  cases are for CSV forcing only in correspondence with the available reference data. The scalar is concentrated in the vicinity of the wall, that is, in the diffusive surface layer with  $\Theta^+ = Sc y^+$  as indicated. A log region can be discerned that appears slightly curved due to double-logarithmic axes. However, the log region runs almost flat for high  $Sc$ . The prominent outer layer ‘spike’ for  $Sc < 1$  and  $y^+ > Re_\tau/2$  disappears for  $Sc \gg 1$ . For constant  $Sc > 1$ , the ODT simulated scalar boundary layer profiles collapse for all  $Re_\tau$  investigated demonstrating

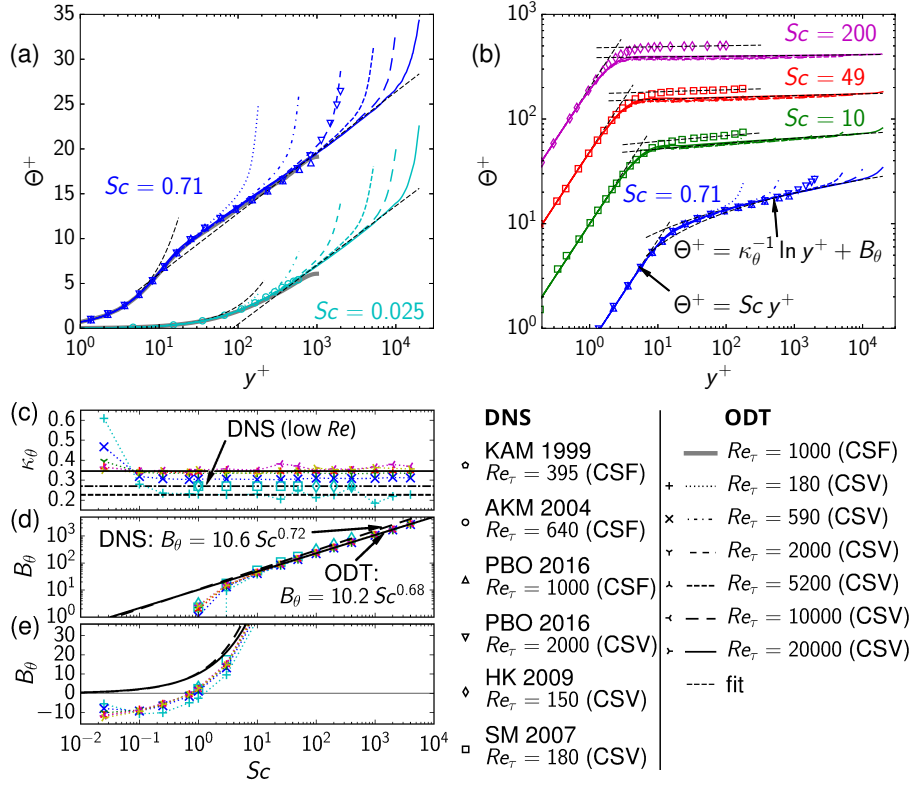


Figure 5: Mean profiles of the normalized scalar,  $\Theta^+$ , for various  $Sc$  and  $Re_\tau$ ; (a) low  $Sc \leq 0.71$  regime in semi-logarithmic, and (b) high  $Sc \geq 0.71$  regime in double-logarithmic scale. Fitted log layer coefficients for  $Sc \geq 0.71$  using an extended data set (CSV forcing); (c) von-Kármán constant,  $\kappa_\theta$ , and (d, e) additive constant,  $B_\theta$ , for high and low  $Sc$ , respectively. Open symbols denote reference DNS results from [1, 2, 4, 5, 39]. Line styles in (a b) and cross-like symbols in (c-e) are used to distinguish ODT profiles and fit coefficients, respectively, for different  $Re_\tau$ . Colors distinguish different  $Sc$  in (a, b), but  $Re_\tau$  in (c-e) analogous to figure 3. Empirical relations, fits, and scaling laws are given by black dashed lines.

that inner scaling holds up to high asymptotic control parameter values. There is no indication of a asymptotic  $Re_\tau$  dependence of the scalar mean field. Note also that the model systematically but proportionally with  $Sc$  underestimates  $\Theta^+$  for  $y^+ > 10$  throughout the log and outer layers. This is due to an overestimation of  $\theta_\tau$  (compare with table 1) that, for fixed wall values (CSV forcing), manifests itself by a systematically lower additive constant  $B_\theta$  as shown previously for small Reynolds numbers [16]. Below, in sections 4.3 and 4.6, we show how this is related to the dissimilarity of the scalar and momentum transfer to the wall that is only partially captured by the model.

In figures 5(c, d) the fitted coefficients  $\kappa_\theta$  and  $B_\theta$ , respectively, of all ODT simulated CSV cases are summarized using double-logarithmic axes. In addition, figure 5(e) shows  $B_\theta$  in semi-logarithmic axes for  $Sc \ll 1$  where  $B_\theta$  is negative such that the diffusive sublayer, which is defined by intersecting log and linear layers (e.g. [5]), ceases to exist. For CSV forcing considered here,  $\kappa_\theta$  drops with  $Sc$  because of the outer layer upward ‘spike’ and, hence, the influence of the bulk diminishes for top of the log layer. Interestingly,  $\kappa_\theta$  retains a notable  $Re_\tau$  dependence for high asymptotic  $Sc$ . For low  $Re_\tau \simeq 180$  investigated,  $\kappa_\theta = 0.27 \pm 0.01$  for DNS [4, 5] and  $\kappa_\theta = 0.23 \pm 0.03$  for ODT when accounting for even higher  $Sc$  than in [16]. For high  $Re_\tau \geq 2000$  investigated, ODT predicts  $\kappa_\theta = 0.35 \pm 0.04$  for high asymptotic  $Sc$  and  $Re_\tau$ . Values seem to approach  $\kappa \approx 0.4$  of the velocity boundary layer (e.g. [32]) which signals that scalar and momentum transport are asymptotically more similar in the bulk fluid across the log and outer layers.

The underestimation of  $B_\theta$  for high asymptotic  $Sc$  is barely notable in figure 5(d) and only revealed by fitting an empirical scaling law,

$$B_\theta(Sc) = A Sc^p , \tag{13}$$

for both available DNS [4, 5] and present ODT results. The prefactor  $A \approx 10$  is similar in DNS and ODT, but the exponent  $p$  is different, that is,  $p \approx 0.72$  for DNS and  $p \approx 0.68$  for ODT. This difference in the parameterization roots in ODT’s overestimation of  $\theta_\tau$  which is related to the similarity of the scalar

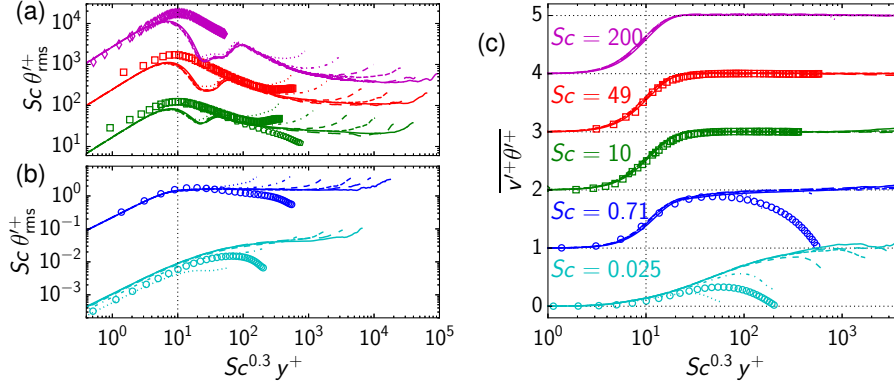


Figure 6: (a, b) Root-mean-square (rms) scalar fluctuation,  $\theta'_{\text{rms}}^+$ , for high and low  $Sc$ , respectively, and (c) wall-normal turbulent scalar flux,  $\overline{v'^+\theta'^+}$ , for various  $Sc$  and  $Re_\tau$ . Note that  $\theta'_{\text{rms}}^+$  and  $y^+$  are pre-multiplied with  $Sc$  and  $Sc^{0.3}$  for visibility and exploitation of scalar boundary layer similarity [5], respectively. A dashed vertical line marks the nominal location of the high  $Sc$  maximum r.m.s. fluctuation that corresponds to the inflection point in the turbulent flux.  $\overline{v'^+\theta'^+}$  is vertically shifted by 1 for visibility as indicated by dashed horizontal base lines. ODT results are for CSV only, whereas reference DNS are for both CSV (turning upward) and CSF (turning downward). Line styles, symbols, and colors as in figures 5(a, b).

360 and momentum transfer (see below) and, hence, the limiting relation for the scalar diffusivity [17, 36]. For low asymptotic  $Sc$  shown in figure 5(e), ODT predicts universal behavior for all  $Re_\tau$ , with  $B_\theta \approx -10$  for CSV forcing and a local logarithmic fit to the scalar profile  $\Theta^+(y^+)$ .

#### 4.2. Scalar fluctuations and turbulent fluxes

365 In addition to the mean field, ODT aims to resolve turbulent fluctuations and provide detailed flow statistics. We therefore use ODT to estimate the variability of all flow variables without additional closure modeling. As a first step in the fluctuation analysis, the variability and turbulent transport in the turbulent boundary layer is addressed below for the passive scalar.

370 Figures 6(a, b) show wall-normal profiles of the normalized r.m.s. scalar fluctuation,  $\theta'_{\text{rms}}^+ = (\overline{\theta^2} - \Theta^2)^{1/2}/\theta_\tau$ , for various  $Re_\tau$  and  $Sc$  along with available reference DNS results. These fluctuations notably increase with  $Sc$  at small finite wall distance and towards the bulk for large  $y^+$  in the case of CSV, whereas

they reduce towards the bulk in the case of CSF forcing. For  $Sc = 10$ , reference  
 375 data for CSV [5] and CSF [1] exhibit perfect inner layer similarity. This simi-  
 larity is almost everywhere reproduced by ODT so that we limit our attention  
 to CSV forcing for all other ODT cases shown. Exceptional ODT behavior is  
 limited to a finite but small wall-distance interval,  $5 < Sc^{0.3} y^+ < 100$ , for large  
 $Sc$ . For increasing  $Sc > 1$ , a near-wall fluctuation peak develops at nominal  
 380 location  $Sc^{0.3} y^+ \approx 10$  [4, 5] that is indicated by a dotted line. The peak width  
 and location obey inner scaling arguments and are well-captured by ODT, but  
 its shape and maximum are not. The latter is a modeling artifact that is re-  
 lated to the triplet map (5) used as an eddy micro-structure model to evaluate  
 equations (4) and (9). This is discussed in [25] for the inner  $u'_{\text{rms}}^+$  peak shown  
 385 in the above figure 3(c). By model analogy, the artifact manifests itself also  
 in the scalar fluctuations that are governed by the velocity boundary layer for  
 $Sc > 1$ . Hence, ODT aims to resolve transient wall-normal transport processes  
 but is unable to resolve effects related to stream- and span-wise turbulent flow  
 structures (e.g. [4]).

390 Figure 6(c) shows the turbulent scalar flux,  $\overline{v'^+ \theta'^+}$ , which is estimated di-  
 rectly from the ensemble of discrete eddy events as described in Appendix B  
 below. ODT accurately captures the turbulent scalar flux for high asymptotic  
 $Sc$  in agreement with reference DNS [5] up to  $Sc = 49$ . The inflection point is  
 located at  $Sc^{0.3} y^+ \approx 10$ , which is consistent with the location of the peak in  
 395  $\theta'_{\text{rms}}^+$  even though ODT does not fully capture the latter peak up to  $Sc = 200$   
 shown. The turbulent scalar flux approximately reaches 1 at some wall distance  
 irrespective of the forcing used for  $Sc \geq 0.71$  investigated. This demonstrates  
 surface layer similarity and dominance of turbulent transport at high  $Sc$ . To-  
 wards the bulk, the turbulent scalar flux therefore depends on the scalar forcing  
 400 used, that is,  $\overline{v'^+ \theta'^+}$  reaches a constant for CSV forcing, and turns down for  
 CSF forcing.

For the low but finite  $Sc = 0.025$  investigated, the behavior is qualitatively  
 different because scalar diffusion now heavily interacts with turbulent advection  
 that enhances mixing across the turbulent boundary layer; this is addressed be-

405 low in see section 4.5. Irrespective of the forcing used, the turbulent scalar flux reaches a local maximum and turns downward towards the bulk. ODT predictions and reference DNS [1, 39] are in agreement for  $Re_\tau \geq 180$  investigated, yielding a universal surface layer region  $Sc^{0.3}y^+ < 20$  for which the turbulent fluxes of all reference and simulated cases collapse.

410 *4.3. Probability density function of surface fluxes*

Conventional statistics discussed above have revealed that ODT is able to reasonably capture low-order statistical moments of the velocity and scalar boundary layer. This fundamental property is relevant, but might as well be achieved with conventional sub-filter scale closure modeling for the given application. However, for modeling multiphysics boundary-layer flows it is also crucial to accurately capture detailed state-space statistical properties like correlations. The ODT model has already been applied to such problems (e.g. [12–14]). Hence, wall-bounded scalar turbulence in channel flow serves as a canonical example in which the correlation of surface scalar and momentum fluxes has been documented in the literature.

Surface fluxes are resolved by the ODT model and they are obtained as time series of the fluctuating wall gradients of transported property fields. These wall gradients are chaotically perturbed by the turbulent boundary layer above the wall. Bulk quantities (like the temperature, or the turbulent drag that arises from the pressure drop across a channel segment) are very sensitive to the corresponding surface fluxes and their variability. The relevant flux quantities are the instantaneous stream-wise wall-shear stress fluctuations,  $\tau'_w = \tau_w - \bar{\tau}_w$ , and the instantaneous surface scalar flux fluctuations,  $q'_w = q_w - \bar{q}_w$ . These quantities are obtained from ODT simulations as an ensemble of time-series,

$$\tau'_w = \nu \frac{\partial u'}{\partial y} \Big|_w, \quad q'_w = \Gamma \frac{\partial \theta'}{\partial y} \Big|_w. \quad (14a, b)$$

Figure 7 shows joint probability density functions (jPDFs) of the instantaneous stream-wise wall-shear stress and the surface scalar flux fluctuations for  $Sc = 0.71$  and  $Sc = 0.025$ , respectively, for fully-developed turbulent channel

flow with  $Re_\tau = 1000$  and CSF forcing of the scalar. Sixty bins were used  
 425 in each direction over the indicated bounds in computing the jPDFs for ODT  
 simulations. ODT model predictions are shown in comparison with available  
 reference DNS results [1]. The ODT model is able to capture relevant features  
 of the reference DNS distribution functions for the same physical parameters  
 and fixed model calibration. The locations of the maxima and the spread around  
 430 them are particularly well captured, which is consistent with the fidelity of the  
 low-order statistical moments discussed above.

There are two notable discrepancies between the present ODT and reference  
 DNS results. One is the slightly narrower jPDF for moderate  $Sc = 0.71$  and  
 more localized jPDF for small  $Sc = 0.025$ , which indicates somewhat stronger  
 435 correlation of the momentum and surface scalar fluxes in the model than in the  
 DNS. We attribute this to the near-wall triplet mapping in wall-attached eddy  
 events that result in almost identical manipulations of the scalar and shear-  
 dominating stream-wise velocity profiles there.

Another discrepancy is the missing negative surface scalar flux contributions  
 440 (below -1) for low  $Sc = 0.025$ , which surprisingly is not an issue at  $Sc = 0.71$ .  
 For small  $Sc$ , or, more precisely, small friction Peclet numbers,  $Pe_\tau = Sc Re_\tau \lesssim$   
 1, the scalar property field relaxes faster by molecular diffusion than it is stirred  
 by turbulent eddies. When the next wall-attached eddy occurs, the near-surface  
 profile is already relaxed to a smooth monotonic profile. Triplet mapping of such  
 445 monotonic profiles can only increase the wall gradient but it can never reverse  
 it. The scalar wall gradient and, hence, the surface scalar flux fluctuation, can  
 not fall substantially below zero for  $Pe_\tau \ll 1$ . We emphasize that the low  
 $Sc = 0.025$  case is not constrained below  $q'_w/q_{w,rms} = 0$ , it is constrained below  
 -1. Hence, there is quite a bit of negative wall fluctuation. The above argument  
 450 implies that stronger negative scalar flux fluctuation in the DNS is due to the  
 more complex three dimensional eddy structure [4] that is not fully resolved by  
 ODT.

Note that the wall fluxes are not actually negative, they are negative fluctu-  
 ation about the mean. Adopting inner scaling, equation (2), the ODT simulated

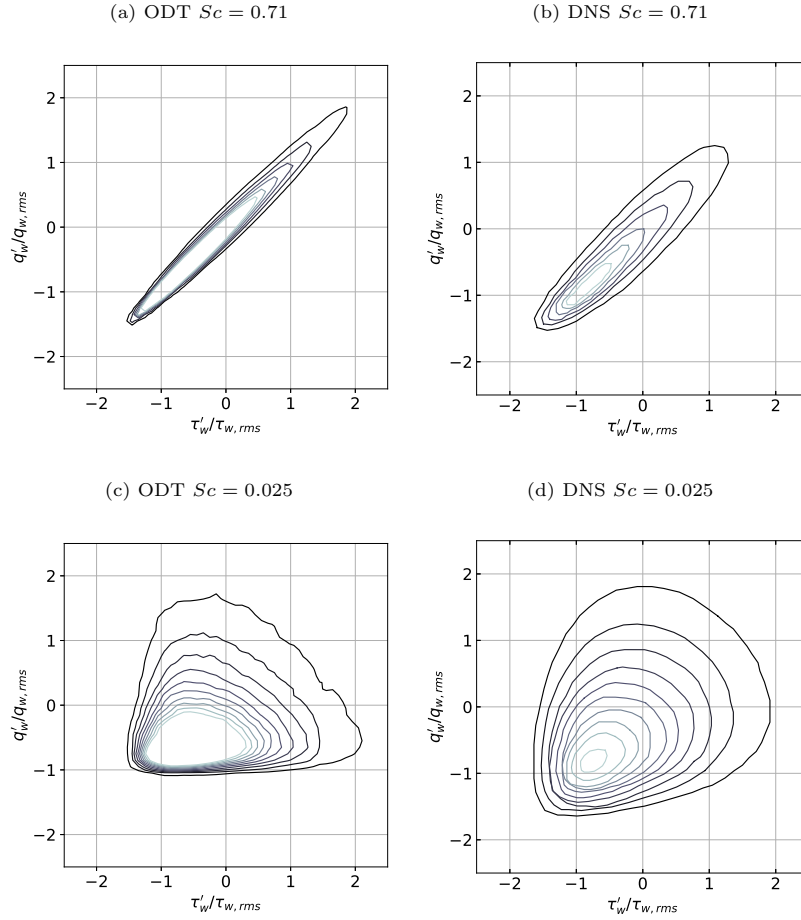


Figure 7: Joint probability density functions (jPDFs) of the wall shear stress fluctuations,  $\tau'_w$ , and surface scalar flux fluctuations,  $q'_w$ , at the channel wall (w) for  $Re_\tau = 1000$  (CSF). Fluctuating quantities are normalized by the respective root mean square (rms) values. Probability density contours are shown starting at and spaced by 0.1 for  $Sc = 0.71$ , and starting at and spaced by 0.025 for  $Sc = 0.025$ . Corresponding reference DNS results are from [1].

455 mean and r.m.s. values are  $\bar{\tau}_w^+ = 1$  and  $\tau_{w,\text{rms}}^+ = 0.363$ , along with  $\bar{q}_w^+ = 19.33$   
 (19.60) and  $q_{w,\text{rms}}^+ = 7.49$  (7.81) for  $Sc = 0.71$  (0.025). The jPDF of the to-  
 tal surface fluxes can be obtained by shifting the origin by  $\bar{\tau}_w/\tau_{w,\text{rms}}' = 2.74$   
 and  $\bar{q}_w/q_{w,\text{rms}}' = 2.58$  (2.51), respectively. Note further in this respect that the  
 460 stream-wise wall-shear stress, that is, the total instantaneous momentum flux,  
 may drop below zero due to the kernel mechanism, equations (4, 7), that acts  
 in addition to the triplet mapping and models the effects of pressure-velocity  
 correlations for any nonzero value of the model parameter  $\alpha$ . Indeed, the extent  
 of the negative viscous stress is very similar between the ODT and the DNS.  
 However, negative stresses are extremely rare.

465 By contrast to what was just described, for moderate and large  $Sc$ , or more  
 precisely,  $Pe_\tau = Sc Re_\tau \gtrsim 1$ , a cascade of eddy events can fit within the diffusion  
 time scale. This means that a non-monotonic scalar profile due to a large eddy  
 event is propagated to the wall by subsequent smaller events in the cascade.  
 This constitutes a mechanism for counter-gradient fluxes across the boundary  
 470 layer that can lead to temporary negative wall gradients and surface fluxes.

While noting the differences in the jPDFs between the ODT and the DNS  
 due to the mixing phenomenology of the ODT, and of course the lack of three-  
 dimensional flow structures in the ODT, the overall qualitative agreement is  
 quite remarkable given the relative simplicity of the ODT simulations. These  
 475 results serve to highlight the importance and sensitivity of physical processes  
 occurring in the flow that can be difficult to isolate with a single model that is  
 constrained in its representation of the flow (even if such constraint is physically  
 realistic, as in the case of DNS).

#### 4.4. Scalar variance budget

The scalar variance budget is primarily useful to elucidate the missing scalar  
 fluctuations at high  $Sc$  (see figure 6(a) above). But, in general, the scalar vari-  
 ance budget will help us to obtain a quantitative understanding of the fluctu-  
 ating passive scalar transport in comparison to the TKE (see figure 4). The  
 scalar variance transport equation that defines the budget of terms is given by

(see e.g. [5])

$$\frac{\partial \overline{\theta'^2}}{\partial t} + \mathbf{U} \cdot \nabla \overline{\theta'^2} = P_\theta + \varepsilon_\theta + D_\theta + T_\theta, \quad (15)$$

where  $\overline{\theta'^2} = \theta_{\text{rms}}'^2$  denotes the scalar variance,  $P_\theta$  the production,  $\varepsilon_\theta$  the dissipation,  $D_\theta$  the diffusive transport, and  $T_\theta$  the turbulent transport of the scalar variance. The left-hand side vanishes for statistically stationary channel flow, and the terms on the right-hand side only retain their wall-normal contributions within the ODT modeling framework, that is,

$$P_\theta = -2\overline{v'\theta'} \frac{d\Theta}{dy}, \quad \varepsilon_\theta = -2\Gamma \frac{\partial \theta'}{\partial y} \frac{\partial \theta'}{\partial y}, \quad D_\theta = \Gamma \frac{d^2 \overline{\theta'^2}}{dy^2}, \quad T_\theta = -\frac{d \overline{v'\theta'^2}}{dy}. \quad (16a, b, c, d)$$

480 The corresponding nondimensional expressions for these terms are obtained by division with  $\theta_\tau^2 u_\tau^2 / \nu$ , which is indicated by the super-script ‘+’.

Figures 8(a–c) show the normalized scalar variance budget balance for both ODT and reference DNS for  $Sc = 0.7$ ,  $Sc = 49$ , and  $Sc = 0.025$ , respectively. The nondimensional terms are additionally normalized for each case with the  
 485 corresponding peak production,  $P_{\theta, \text{max}}^+ = Sc/2$  [5]. ODT exhibits a balance of the scalar variance budget as the right-hand-side terms of equation 15 sum to zero. The gross structure of all terms is captured by ODT, but somewhat better for the lower  $Sc = 0.7$  than for the higher  $Sc = 49$ , and generally less well for low  $Sc = 0.025$ .

490 For moderate and high  $Sc$ , figures 8(a,b), the turbulent production peak is correctly predicted with some discrepancy in its tail as the  $Sc$  number increases. At the same time, dissipation is increasingly underestimated so that compensating transport maintains the balance. The compensation is primarily achieved by turbulent transport and less by diffusive transport. This is consistent with  
 495 the previously discussed modeling artifacts in the r.m.s. fluctuation for large  $Sc$ .

For low  $Sc$ , figure 8(c), ODT still exhibits a balance, but now both production and dissipation are overestimated in magnitude whereas the turbulent and diffusive variance fluxes are reasonably well captured. We attribute the former  
 500 to the triplet mapping (5) in the discrete eddy events. Small-scale scalar vari-

ance is artificially enhanced by instantaneous mappings that introduce profile gradient discontinuities that are quickly regularized by deterministic molecular diffusion due to which the scalar variance dissipation is also artificially increased. This reveals the relevance of resolving the time-scale separation between turbulent advection and molecular diffusion. Interestingly, this is a local effect that is almost balanced due to time-scale separation between turbulent advective and molecular diffusive transport processes for  $Sc \ll 1$ . This separation is resolved by ODT such that the turbulent fluxes of the scalar fluctuation variance are well captured by the model, albeit production and dissipation are not. Below, we address ODT’s capabilities for capturing fluid-surface interactions of turbulent mixing in wall-bounded flows.

#### 4.5. *Mixing time scale*

Physical processes in boundary-layer flows are sensitive not only to near-wall fluctuations and turbulent transport but also to the local mixing efficiency. In particular, this is the case for flows that exhibit intense scalar-wall interaction (like wall fires [14] or scalar mixing processes in the atmospheric surface layer [37]). In the following, we therefore address ODT’s capabilities for capturing molecular mixing processes and fluctuation damping for various independent  $Sc$  number scalars in the vicinity of a wall under turbulent flow conditions. The related mixing efficiency is quantified by the mixing-time-scale ratio,  $R$ , that is given by

$$R = \frac{\overline{\theta'^2}/\varepsilon_\theta}{2k/\varepsilon},$$

where  $k$  denotes the turbulence kinetic energy (TKE) and  $\varepsilon$  the TKE dissipation in the lower-order model as defined in equation (11).

Figure 9 shows wall-normal profiles of the mixing-time-scale ratio,  $R$ , by comparing ODT predictions with reference DNS and both are found to exhibit reasonable agreement. Due to inner layer similarity discussed above in sections 4.1, 4.2, and 4.4, only ODT results with CSV forcing are shown for low  $Re_\tau$  that correspond with available reference DNS. The vicinity of the wall is dominated by molecular diffusion which is why  $R \rightarrow Sc$  for  $y^+ \rightarrow 0$  for any finite

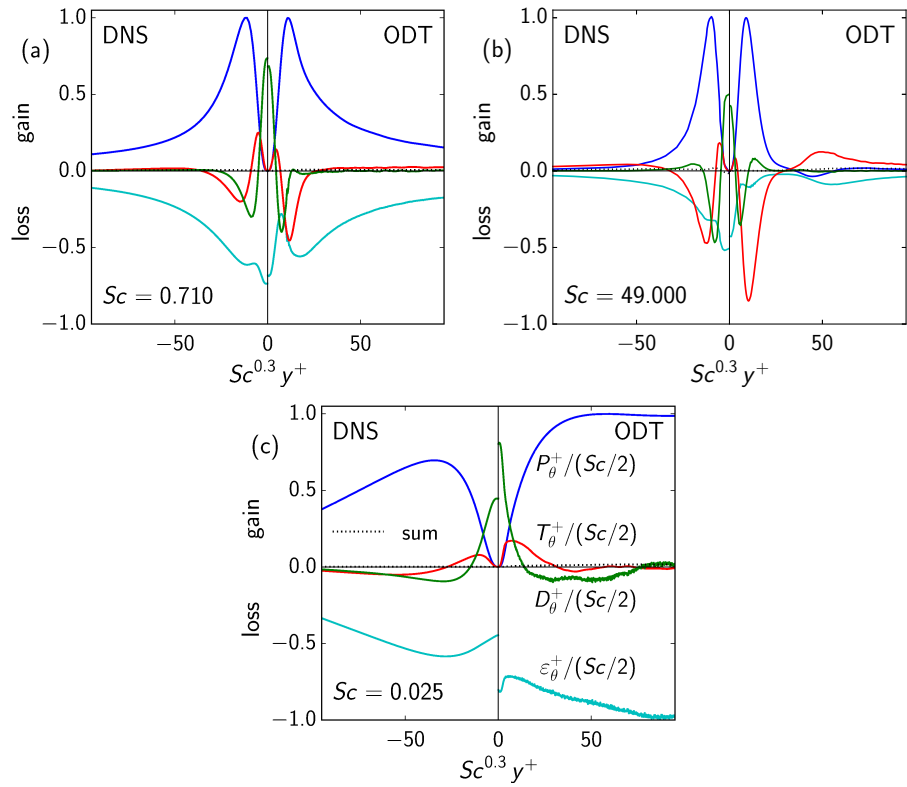


Figure 8: ‘Back-to-back’ plot of the scalar variance budget balance given by equation (16) for ODT ( $y^+ \geq 0$ ) and equation (15) for reference DNS ( $y^+ \leq 0$ ). (a)  $Sc = 0.7$ , ODT:  $Re_\tau = 590$  (CSV), DNS:  $Re_\tau = 640$  (CSF) [39]; (b)  $Sc = 49$ , ODT:  $Re_\tau = 180$  (CSV), DNS:  $Re_\tau = 180$  (CSV) [5]; and (c)  $Sc = 0.025$ , ODT:  $Re_\tau = 590$  (CSV), DNS:  $Re_\tau = 640$  (CSF) [39].

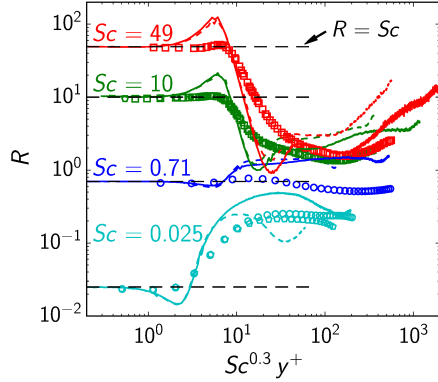


Figure 9: Mixing-time-scale ratio,  $R$ , from equation (17) across the turbulent boundary layer for various  $Sc \leq 49$  and  $Re_\tau \leq 640$  for visibility. Line styles, symbols, and colors as in figures 5(a, b).

$Sc$  and  $Re_\tau$ . With increasing distance from the wall, that is, for  $Sc^{0.3}y^+ > 10$ , we find  $R \simeq 1$  which is consistent with the analysis of the turbulent boundary-layer structure (section 4.1) that the scalar and momentum transport tend to be more similar towards the bulk. Across the log layer, both scalar and momentum  
525 (velocity) mixing is dominated by the inertial range of the turbulence cascade. For even larger distances from the wall, specifics of the outer layer and bulk flow influence the mixing behavior. Note in this regard that the diffusion-dominated scalar surface layer thickness decreases like  $Sc^{-0.3}$  (e.g. [4, 36]) such that it becomes negligibly small for  $Sc \rightarrow \infty$  in relation to the viscous sublayer with  
530 thickness  $y^+ \approx 5$  (e.g. [30]). The scalar transfer and mixing properties are then dominated by the momentum boundary layer (e.g. [36, 40]).

#### 4.6. Sherwood number and scalar transfer coefficient

We have shown above that ODT resolves transient transport processes in the whole boundary layer including surface flux fluctuations. An important  
535 remaining question that we address in this section is: how well can ODT capture and predict the scalar transfer to a wall?

Scaling regimes of the scalar transfer to a wall are quantified by the Sherwood number,  $Sh \sim q/q_\Gamma$ , which expresses the total scalar flux,  $q$ , in units of the purely

molecular diffusive flux,  $q_\Gamma$ , under (assumed) absence of turbulence and up to  
540 a multiplicative constant. The Sherwood number is the analog of the Nusselt  
number in the context of mass rather than heat transfer that is here generalized  
as scalar transfer. When temperature variations are small and internal heating  
due to viscous dissipation negligible (which is often justifiable), both Sherwood  
and Nusselt numbers are isomorphic, in particular with respect to their scaling  
545 laws. In this study, either  $q$  is directly prescribed by  $q_w$  in the case of isoflux  
wall-boundary conditions (CSF forcing) or it is obtained as model result in the  
case of Dirichlet wall-boundary conditions (CSV forcing). For CSV forcing,  
that is considered in more detail in the following,  $q_\Gamma$  is proportional to the  
prescribed bulk-wall (half wall-to-wall) scalar difference,  $\Delta\theta = |\theta_{\text{top}} - \theta_{\text{bot}}|/2$ ,  
550 yielding  $q_\Gamma = \Gamma \Delta\theta/\delta$  for channel flow as sketched in figure 1(a).

For fully-developed channel flow, the total scalar flux is carried by molec-  
ular diffusion such that  $Sh$  is related to the scalar transfer coefficient,  $K^+$ , as  
(e.g. [40, 41])

$$Sh = \gamma Re_\tau Sc K^+(Re_\tau, Sc), \quad K^+ = \theta_\tau/\Delta\theta, \quad (18a, b)$$

in which  $\gamma$  denotes a conventional geometrical proportionality constant and  $\theta_\tau$   
the friction scalar property defined in equation (2b). Following [5], we select  
 $\gamma = d_h/(2\delta) = 2$ , which implies  $Sh$  based on the hydraulic diameter,  $d_h = 4\delta$ ,  
rather than the channel half-width  $\delta$ . A conventional Nusselt number, therefore,  
555 is  $Nu = Sh$  (e.g. [1, 2, 42]) that exhibits the same  $Sc$  and  $Re_\tau$  dependence as  
 $Sh$ .

Figures 10(a, b) show  $K^+$  and  $Sh$ , respectively, for various  $Sc$  number passive  
scalars in turbulent channel flows at different  $Re_\tau$ . ODT predictions are shown  
together with available reference DNS, pipe flow measurements (filled gray bul-  
560 lets) [36], and empirical scaling relations. Three different scaling regimes of the  
scalar transfer can be discerned, corresponding to low, intermediate, and high  
 $Sc$ . ODT results exhibit very good to reasonable agreement with the reference  
data and scaling relations that seems to improve for high asymptotic  $Re_\tau$ . We  
proceed in the following by addressing the scaling regimes individually.

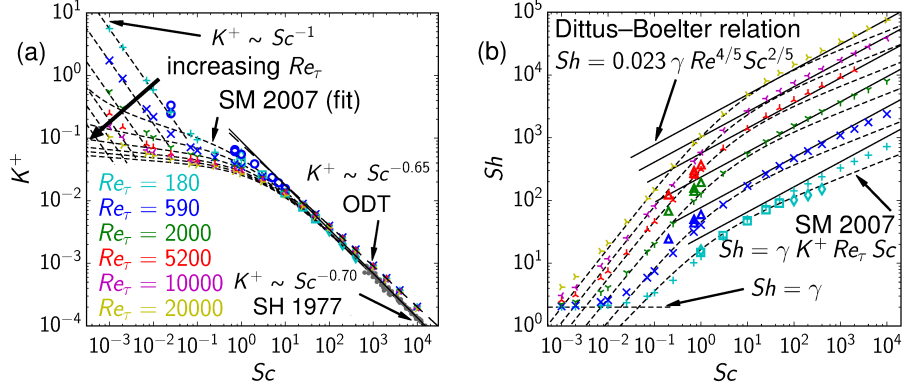


Figure 10: Dimensionless scalar transfer in terms of the (a) the scalar transfer coefficient,  $K^+$ , and (b) Sherwood number,  $Sh$ , as functions of  $Sc$  for various  $Re_\tau$ . Reference empirical scaling relations for  $K^+$  and  $Sh$  are based on equations (18), (19), and (21). Symbols and colors as in figures 5(c-e).

565 We first discuss the diffusive limit,  $Sh \rightarrow \gamma = 2$  for  $Sc \rightarrow 0$ , that exhibits an increasing time-scale separation that makes numerical simulations costly or barely feasible for applications such as heat transfer in liquid metal batteries (e.g. [43]). ODT can accommodate large time-scale separation. For constant  $Sh$ , equations (2) and (18) yield the presence of a purely diffusive scalar profile.

570 For CSV forcing, this profile is steady and linear yielding  $K^+ \rightarrow Sc^{-1} Re_\tau^{-1}$ . Hence,  $Sh$  becomes parametrically independent of  $Re_\tau$  for asymptotically small  $Sc$ . This is fulfilled in practice for any small friction Peclet number,  $Pe_\tau = Re_\tau Sc \ll 1$ . The latter condition limits the maximum permissible friction Reynolds number to  $Re_\tau \ll Sc^{-1}$  for diffusion-dominated scalar transfer.

575 We now turn to the high  $Sc$  and  $Re_\tau$  flow regime that is relevant for various applications but numerically inaccessible due to high computational resource requirements that are imposed by the Kolmogorov and Batchelor scales as well as the sampling time (e.g. [2, 5, 6]). A lower-order model like ODT makes small-scale resolving numerical simulations feasible. The model aims to resolve

580 fluctuating wall-normal molecular and turbulent transport processes on all relevant scales such that the mean scalar transfer is a model result. Reference

empirical scaling relations are available that were obtained by measurements and theoretical considerations (e.g. [40, 41, 44, 45]). Some widely used scaling relations expressed in terms of the  $Sc$  and  $Re$  dependence of  $Sh$  take the form  
 585 of a power law,

$$Sh \simeq 0.023 \gamma Re^{4/5} Sc^b, \quad (19)$$

where  $b = 2/5$  yields the Dittus–Boelter relation [46],  $b = 1/3$  the well-established Colburn relation (e.g. [36, 47]), and  $b = 1/2$  a relation that is closer to the Prandtl number dependence of convective heat transfer (e.g. [48]). Note that  $Re = u_b \delta / \nu$  denotes the bulk Reynolds number. For fully-developed turbulent channel flow,  $Re$  can be obtained from the empirical relation  $Re_\tau \simeq$   
 590  $0.18 Re^{0.88} \sim Re^{7/8}$  [30]. ODT exhibits the same scaling exponent, but the prefactor is  $\approx 0.16$  due to underestimation of the velocity in the outer layer (see figure 3(a)). The ODT results shown in figure 10 for  $Sc \gtrsim 10$  fall between the Dittus–Boelter and Colburn relations with a tendency towards the former.  
 595 This is consistent with the ODT limiting relation  $K^+ \sim Sc^{-0.65}$  [16, 17] that is slightly different from the reference  $K^+ \sim Sc^{-0.70}$  [4, 5, 36].

It is apparent by now that finite  $Sc$  and  $Re$  effects play a role for the intermediate scaling regime. These effects were already addressed by Sleicher and Rouse [44], who provided an empirical scaling relation together with the applicability region as

$$Sh = 5 + 0.15 Re^a Sc^b \quad (20)$$

$$\text{with } a = 0.88 - \frac{0.24}{4 + Sc}, \quad b = \frac{1}{3} + \frac{e^{-0.6 Sc}}{2}$$

$$\text{for } Sc \in [10^{-1}, 10^4], \quad Re \in [10^4, 10^6].$$

The above relation is given for completeness of the discussion since it is widely used to address finite  $Sc$  effects (e.g. [42]) Here, we do *not* show equation (20) explicitly in the figures because of the following two reasons. First,  $Sh$  given  
 600 in equation (20) reaches the physically incorrect limit  $Sh \rightarrow 5$  for  $Sc \rightarrow 0$ , which is already notable for moderately low  $Sc \simeq 10^{-1}$ . Second, the above parameterization yields  $Sh \sim Sc^{1/3}$  for  $Sc \rightarrow \infty$ , which is simply the Colburn

scaling that is readily included in a more generally applicable and physically based parameterization that is discussed next.

Schwertfirm and Manhart [5] used DNS in conjunction with turbulent boundary-layer theory to yield the semi-empirical scaling

$$K^+ = \frac{Sh}{\gamma Re_\tau Sc} = \frac{\kappa_\theta}{\ln Re_\tau + \kappa_\theta \xi Sc^{1-r} + r \ln Sc - \ln \xi} \quad (21)$$

$$\text{with } \kappa_\theta = 0.27, \quad \xi = 11.5, \quad r = 0.29 \quad \text{for } Sc \gtrsim 1.$$

605 In this equation, the logarithmic correction emerges due to the presence of scalar inner linear and log layers. The analysis put forward by [5] is strictly valid only for  $Sc \gtrsim 1$  such that the linear and log layer scalar profiles intersect as can be seen in figure 5(a, b) for  $Sc \geq 0.71$ . This intersection unambiguously defines a diffusive scalar boundary layer thickness, which, for asymptotically high  $Sc$ , takes the form  $\delta_\Gamma^+ \simeq \xi Sc^{-r}$ , where  $r \approx 0.3$  [5, 36]. Note that the value of  $r \approx 0.3$  corresponds with the similarity scaling of the scalar boundary layer coordinate,  $Sc^{0.3} y^+$ , that was used in various figures above. Note further that  $r$  in the asymptotic relation for  $\delta_\Gamma^+$  implies that  $Sh$  due to equation (21) approaches the Colburn scaling,  $Sh \sim Sc^r \approx Sc^{1/3}$  (e.g. [47]), for high asymptotic  $Sc$ .

615 Relation (21) is shown in figure 10 with thin curved dashed lines that serve for orientation and as bound on the scalar transfer for extrapolated  $Sc < 1$ . To the best of our knowledge, no generalized and physically based relation is currently available for this regime. (Equation (20), for example, fails to capture the limiting behavior for  $Sc \lesssim 10^{-1}$  as discussed above.) The fitting parameters are from [5] and were obtained with the aid of DNS for turbulent channel flow at  $Re_\tau = 180$  with  $Sc < 50$  passive scalars using CSV forcing. This parameterization predicts  $K^+$  for another DNS at  $Re_\tau = 150$  for  $Sc \leq 400$  [4] and measurements in pipes with for high asymptotic  $Re_\tau$  and  $Sc$  of the order  $10^3$  to  $10^4$  [36]. ODT captures this behavior but would yield somewhat different numerical fitting parameters due to the marginally captured emerging dissimilarity of the near-surface scalar and momentum transport [16, 17]. The origin of this effect is discussed above in sections 4.1, 4.3, and 4.4, showing that it is related to the resolved and unresolved model physics. We note that, for

finite  $Re_\tau$  and  $Sc$ , ODT results are well described by relation (21). This implies  
 630 that local effective scalings,  $Sh \sim Sc^b$ , with  $b > 2/5$  are realized that are  
 steeper than the Dittus–Boelter and Colburn relations [49]. This demonstrates  
 the model’s capabilities for capturing regime transitions in scalar transfer by  
 resolving a relevant fraction of the state space of surface-flux fluctuations.

## 5. Conclusion

635 One-dimensional turbulence (ODT) numerical simulations of passive scalars  
 turbulent channel flow have been performed up to  $Re_\tau = 20,000$  for  $Sc \in$   
 $[10^{-3}, 10^4]$  with the scalar prescribed either by constant scalar value (CSV) or  
 constant scalar flux (CSF) wall-boundary conditions. These simulations were  
 made feasible by utilizing a fully-adaptive ODT implementation as stand-alone  
 640 tool that aims to resolve transient wall-normal transport processes on all rel-  
 evant flow scales within a lower-order stochastic framework. The free model  
 parameters were calibrated once for the velocity boundary layer such that the  
 $Sc$  and  $Re_\tau$  dependencies reported are model predictions. ODT consistently  
 predicts low-order flow statistics throughout the boundary layer with perfect  
 645 surface (inner) layer similarity irrespective of the scalar forcing used. Wall-  
 normal fluxes are very well captured, but the model fails to resolve some fluctu-  
 ations that are related to stream- and span-wise flow structures. This modeling  
 error manifests itself by an unphysically degraded local near-wall scalar fluctu-  
 ation maximum and an overestimation of the scalar wall-gradient for CSV and  
 650  $Sc \gg 1$ . Nevertheless, the ODT solutions obey inner scaling and collapse for all  
 $Re_\tau$  investigated. Joint probability density functions (jPDFs) of the fluctuat-  
 ing wall-shear stress and surface scalar flux reveal that the negative scalar flux  
 fluctuations are more constrained in ODT than in DNS. This is another man-  
 ifestation of the dimensional modeling error since the three-dimensional eddy  
 655 structure in the DNS that can support the negative scalar flux fluctuations, but  
 not the map-based advection model that is used in ODT. Nevertheless, ODT is  
 able to accurately capture local mixing time scales which is a crucial property

for application to multiphysics boundary layers. Finally, it was shown that the model is able to accurately predict the scalar transfer to the surface which is  
660 quantified by the Sherwood (Nusselt) number,  $Sh(Sc, Re_\tau)$ . Present ODT re-  
sults reproduce the scaling relation proposed by Schwertfirm and Manhart [5]  
for finite  $Re_\tau \geq 180$ ,  $Pe_\tau = Sc Re_\tau \geq 20$ , and  $Sc \leq 100$ . This relation is based  
on boundary-layer theory and is, thus, superior to any purely empirical relation  
(like the one from Sleicher and Rouse [44]). For small asymptotic  $Sc < 20 Re_\tau^{-1}$   
665 ( $Pe_\tau < 20$ ), there is currently no theory available but ODT consistently ex-  
trapolates  $Sh$  to the diffusive limit. For high asymptotic  $Sc$ , ODT results fall  
between the Dittus-Boelter,  $Sh \sim Sc^{2/5}$ , and Colburn,  $Sh \sim Sc^{1/3}$ , scalings  
but they are closer to the former than the latter, albeit this is approached by  
the relation from Schwertfirm and Manhart [5]. Complex three-dimensional flow  
670 structures are not fully captured by the model but it can now be confidently  
applied to multiphysical wall-bounded flows for which surface-flux fluctuations  
and transient wall-normal transport processes are crucial.

### Acknowledgements

We thank Alan Kerstein for fruitful discussion.

675 Funding: M.K. and H.S. acknowledge financial supported by the European  
Regional Development Fund [grant number StaF 23035000].

The fully-adaptive ODT implementation used for this study is publicly avail-  
able at the following URL: <https://github.com/BYUignite/ODT>.

### Appendix A. Scalar forcing by isothermal and isoflux boundary con- 680 ditions

Two scalar forcing methods are considered in this study that are sketched in  
figure 1. In the first, the scalar is prescribed by fixed wall values,  $\theta(y = 0) = \theta_{\text{bot}}$   
at the bottom and  $\theta(y = 2\delta) = \theta_{\text{top}}$  at the top, respectively. This case is  
denoted as CSV (constant scalar value). The scalar forcing term vanishes for  
685 this configuration so that  $s_\theta = 0$  in equation (1b). The ODT domain is fixed

at some location of the channel and flow statistics are gathered in time for an  $M \geq 1$  ensemble of independent flow realizations.

In the second forcing method, the scalar is prescribed by an isoflux wall-boundary condition and is denoted as CSF (constant scalar flux). This configuration yields a linear increase of the bulk scalar property downstream,

$$\Theta_b = q_w t = q_w x / U_d, \quad (\text{A.1})$$

where  $q_w$  is the (constant) prescribed surface scalar flux into the flow domain,  $t$  the elapsed simulation time,  $x$  the downstream distance, and  $U_d$  a constant displacement velocity of the ODT domain. With these boundary conditions a temporal ODT simulation would result in a solution that implies a displacement of the ODT domain downstream with constant mean velocity  $U_d$ , as indicated by two small horizontal arrows in figure 1(b). This corresponds with previous applications of the *temporal* ODT formulation (e.g. [22, 23]) where  $U_d$  was prescribed by the bulk velocity. This is also a common approach when post-processing temporal ODT simulation results for comparison to spatial experimental data. This differs somewhat from the *spatial* ODT formulation (e.g. [10, 14]) that uses the local stream-wise velocity in spatially advancing the ODT line in an assumed steady flow that is, nevertheless, punctuated by instantaneous eddy events. However, the spatial ODT formulation can not be straightforwardly applied to internal flows [13].

As a consequence of these limitations, we apply only the temporal formulation for this study. To facilitate this, the scalar transport equation is modified to compensate for the linear dependence in equation (A.1) by a transformation of variables, as has been previously applied in DNS studies [1, 24].

For the sake of argument, consider the scalar transport equation specialized to the temperature  $T$ ,

$$\frac{\partial T}{\partial t} + \mathbf{u} \cdot \nabla T = \Gamma \nabla^2 T, \quad (\text{A.2})$$

where  $\Gamma$  is the thermal (scalar) diffusivity. In statistically stationary channel flow with a constant and uniform wall heat flux applied, the mean temperature profile increases linearly with downstream distance  $x$ . We define  $\theta = \bar{T}_w - T$ ,

where  $\bar{T}_w$  is the mean wall temperature, which increases linearly with  $x$ . This  
 715 gives  $T = \beta x + \bar{T}_{w,0} - \theta$ , where  $\beta = d\bar{T}_w/dx$ , which is constant. This relation is  
 inserted into the transport equation (A.2) to give

$$\frac{\partial \theta}{\partial t} + \mathbf{u} \cdot \nabla \theta = \Gamma \nabla^2 \theta + \beta u, \quad (\text{A.3})$$

where the last term follows from  $\mathbf{u} \cdot \nabla \beta x = \beta u$ . For application in ODT,  
 equation (1) is solved rather than equation (A.3), with source term  $s_\theta = \beta u$   
 and the stochastic term  $\mathcal{E}_\theta$  formally replacing the advection term  $\mathbf{u} \cdot \nabla \theta$ .

720 Note that  $\beta$  can be chosen arbitrarily. Any constant multiplier of  $\beta$  will not  
 affect statistics of  $\theta^+$ . The friction temperature is given by  $T_\tau = \bar{q}_w / (\rho c_p u_\tau)$ ,  
 which is consistent with equation (2b) for  $T = \theta$ . But the mean heat (scalar)  
 flux  $\bar{q}_w$  is proportional to  $\beta$ , as a simple energy (scalar mass) balance over  
 the channel shows. Hence, inner scaling of equation (A.3) with  $T_\tau$  to give a  
 725 transport equation for  $\theta^+$  results in a cancellation of  $\beta$  in the source term. As a  
 consequence, Dirichlet boundary conditions for  $\theta$  are used with  $\theta(0) = \theta(2\delta) = 0$ .

This formulation of the isoflux boundary conditions is particularly conve-  
 nient since a standard transport equation can be solved with a simple source  
 term. This also allows application of the temporal ODT formulation without  
 730 requiring advection of the the ODT line, as noted above.

In equation (A.2),  $u$  in the source term is taken as the local and momentary  
 ODT stream-wise velocity,  $u(y, t)$ . Results of this configuration are presented in  
 sections 4.1 and 4.3. The majority of the results shown use fixed-value (CSV)  
 wall-boundary conditions and only a few are based on the isoflux (CSF) bound-  
 735 ary condition for the purpose of 1-to-1 comparison with reference DNS where  
 necessary. We justify this, as discussed throughout section 4, by boundary  
 layer similarity that is primarily relevant for the modeling of fluctuating surface  
 fluxes.

## Appendix B. Computation of model-resolved turbulent fluxes

740 The wall-normal components of the Reynolds stress tensor,  $\overline{u'_i v'}$ , and the  
 turbulent scalar flux,  $\overline{\theta' v'}$ , are implicitly resolved along the ODT domain. In

order to compute these cross-correlation terms within the model we have to take into account that eddy events have taken the role of turbulent advection. Fluid is displaced along the ODT domain by application of the triplet map given in  
745 equation (5). Turbulent advective transport is thus an ensemble effect of triplet map applications across a range of scales. These mappings are instantaneous but well defined in location,  $y_0$ , and size,  $l$ .

A measure for the duration of a physical eddy turnover to yield a similar manipulation of property profiles is, thus, given by the eddy time scale,  $\tau$ , from  
750 equation (9). This time scale is readily available from the sampling procedure and we estimate the advecting fluctuation velocity as  $l/\tau$ . Now we have to separate the effects of triplet map applications from other processes that change property profiles. This is achieved by a conditional averaging procedure which, however, can *not* be done alone with an instantaneous property profiles. Instead,  
755 a finite time interval (size  $\Delta t_e$ ) is used to perform conditional eddy statistics in order to estimate the model-resolved turbulent fluxes, that is, cross-correlations that involve  $v'$ .

For the statistically stationary state, the ensemble effect of stochastic eddy events may be written as

$$\frac{\overline{\partial v' \phi'}}{\partial y} \approx - \frac{\Delta \phi_e}{\Delta t_e}, \quad (\text{B.1})$$

760 where  $v'$  denotes the ‘real’ velocity fluctuation in the direction of the ODT line and, correspondingly,  $\phi'$  the ‘real’ fluctuation of a transported flow variable, that is, either a velocity component or a scalar. The cumulative map-induced (‘turbulent’) change,  $\Delta \phi_e$ , of variable  $\phi$  is thus given by

$$\Delta \phi_e(y) = \sum_{k=1}^{N_e} [\phi''(y, t_k) - \phi(y, t_k)] \frac{t_k - t_{k-1}}{\Delta t_e}, \quad (\text{B.2})$$

where index  $k$  counts  $N_e$  eddy events during  $\Delta t_e = t_{N_e} - t_0$ , in which  $t_0$  is the  
765 start and  $t_{N_e}$  the end time of the statistics gathering, and  $\phi''$  represents the map-induced changes of  $\theta''$  or  $\mathbf{u}''$  as defined by equations (4a,b).

At last, equation (B.1) is integrated along the ODT domain to yield the

turbulent flux of the transported variable  $\phi$ . We obtain

$$\overline{v'\phi'} \simeq - \int^y \left\langle \frac{\Delta\phi_e}{\Delta t_e} \right\rangle_M dy' \quad (\text{B.3})$$

as wall-normal profile. Here, we have introduced the ensemble average that is  
770 denoted by  $\langle \cdot \rangle_M$  and encompasses  $M = 1, 2, \dots$  flow realizations. Ensemble  
averaging is optional but may be used to converge the fluctuation statistics  
faster by running several ODT simulations of one case in parallel.

## References

- [1] H. Abe, H. Kawamura, Y. Matsuo, Surface heat-flux fluctuations in a  
775 turbulent channel flow up to  $Re_\tau = 1020$  with  $Pr = 0.025$  and  $0.71$ , *Int. J. Heat Fluid Flow* 25 (2004) 404–419.
- [2] S. Pirozzoli, M. Bernardini, P. Orlandi, Passive scalars in turbulent channel  
flow at high Reynolds number, *J. Fluid Mech.* 788 (2016) 614–639.
- [3] J. W. Deardorff, The counter-gradient heat flux in the lower atmosphere  
780 and in the laboratory, *J. Atmos. Sci.* 23 (1966) 503–506.
- [4] Y. Hasegawa, N. Kasagi, Low-pass filtering effects of viscous sublayer on  
high Schmidt number mass transfer close to a solid wall, *Int. J. Heat Fluid  
Flow* 30 (2009) 525–533.
- [5] F. Schwertfirm, M. Manhart, DNS of passive scalar transport in turbulent  
785 channel flow at high Schmidt numbers, *Int. J. Heat Fluid Flow* 28 (2007)  
1204–1214.
- [6] R. Ostilla-Monico, Y. Yang, E. P. van der Poel, D. Lohse, R. Verzicco, A  
multiple-resolution strategy for direct numerical simulation of scalar tur-  
bulence, *J. Comput. Phys.* 301 (2015) 308–321.
- [7] T. Saxton-Fox, B. J. McKeon, Modeling momentum and scalar transport  
790 in a wall-bounded turbulent flow, in: *Proc. 10th Int. Symp. Turb. Shear*

Flow Phen. (TSFP10), volume 1, Chicago, IL, USA, 2017, pp. 1–6. URL: [http://tsfp10.org/TSFP10\\_program/2/332.pdf](http://tsfp10.org/TSFP10_program/2/332.pdf), ID: 4C-2.

- 795 [8] A. Ebadi, J. C. Cuevas Bautista, C. M. White, G. Chini, J. Klewicki, A heat transfer model of fully developed turbulent channel flow, *J. Fluid Mech.* 884 (2020) R7.
- [9] R. Ranjan, S. Menon, Two level simulation of Schmidt number effect on passive scalar transport in wall-bounded turbulent flows, *Phys. Fluids* 33 (2021) 035124.
- 800 [10] A. R. Kerstein, One-dimensional turbulence: Model formulation and application to homogeneous turbulence, shear flows, and buoyant stratified flows, *J. Fluid Mech.* 392 (1999) 277–334.
- [11] A. R. Kerstein, W. T. Ashurst, S. Wunsch, V. Nilsen, One-dimensional turbulence: vector formulation and application to free shear flows, *J. Fluid Mech.* 447 (2001) 85–109.
- 805 [12] A. R. Kerstein, S. Wunsch, Simulation of a stably stratified atmospheric boundary layer using one-dimensional turbulence, *Boundary Layer Meteorol.* 118 (2006) 325–356.
- [13] J. A. Medina M., M. Klein, H. Schmidt, One-dimensional turbulence investigation of variable density effects due to heat transfer in a low mach number internal air flow, *Int. J. Heat Fluid Flow* 80 (2019) 108481.
- 810 [14] E. Monson, D. O. Lignell, M. Finney, C. Werner, Z. Jozefik, A. R. Kerstein, R. Hintze, Simulation of ethylene wall fires using the spatially-evolving one-dimensional turbulence model, *Fire Tech.* 52 (2016) 167–196.
- [15] M. M. Fragner, H. Schmidt, Investigating asymptotic suction boundary layers using a one-dimensional stochastic turbulence model, *J. Turbul.* 18 (2017) 899–928.

- [16] M. Klein, H. Schmidt, Stochastic modeling of passive scalar transport in turbulent channel flows at high Schmidt numbers, in: Proc. 10th Int. Symp. Turb. Shear Flow Phen. (TSFP10), volume 1, Chicago, IL, USA, 2017, pp. 1–6. URL: <http://www.tsfp-conference.org/proceedings/2017/2/368.pdf>, ID: 1B-2.
- [17] M. Klein, H. Schmidt, Stochastic modeling of passive scalars in turbulent channel flows: predictive capabilities of one-dimensional turbulence, in: A. Dillmann, G. Heller, E. Krämer, C. Wagner (Eds.), New Results in Numerical and Experimental Fluid Mechanics XIII, Notes on Numerical Fluid Mechanics and Multidisciplinary Design, Springer Nature, 2021. URL: <https://arxiv.org/abs/2011.04818>, in press.
- [18] R. C. Schmidt, A. R. Kerstein, S. Wunsch, V. Nilsen, Near-wall LES closure based on one-dimensional turbulence modeling, *J. Comput. Phys.* 186 (2003) 317–355.
- [19] E. D. Gonzalez-Juez, R. C. Schmidt, A. R. Kerstein, ODTLES simulations of wall-bounded flows, *Phys. Fluids* 23 (2011) 125102.
- [20] C. Glawe, J. A. Medina M., H. Schmidt, IMEX based multi-scale time advancement in ODTLES, *Z. Angew. Math. Mech.* 98 (2018) 1907–1923.
- [21] A. S. Monin, A. M. Yaglom, *Statistical Fluid Mechanics: Mechanics of Turbulence*, volume 1, MIT Press, Cambridge, Massachusetts, 1971.
- [22] T. Echekki, A. R. Kerstein, T. D. Dreeben, J.-Y. Chen, ‘One-dimensional turbulence’ simulation of turbulent jet diffusion flames: Model formulation and illustrative applications, *Combust. Flame* 125 (2001) 1083–1105.
- [23] M. Klein, C. Zenker, H. Schmidt, Small-scale resolving simulations of the turbulent mixing in confined planar jets using one-dimensional turbulence, *Chem. Eng. Sci.* 204 (2019) 186–202.

- [24] N. Kasagi, Y. Tomita, A. Kuroda, Direct numerical simulation of passive  
 845 scalar field in a turbulent channel flow, *J. Heat Transfer* 114 (1992) 598–  
 605.
- [25] D. O. Lignell, A. R. Kerstein, G. Sun, E. I. Monson, Mesh adaption for  
 efficient multiscale implementation of one-dimensional turbulence, *Theor.*  
*Comput. Fluid Dyn.* 27 (2013) 273–295.
- 850 [26] D. O. Lignell, V. Lansinger, J. Medina, M. Klein, A. R. Kerstein,  
 H. Schmidt, M. Fistler, M. Oevermann, One-dimensional turbulence mod-  
 eling for cylindrical and spherical flows: Model formulation and application,  
*Theor. Comput. Fluid Dyn.* 32 (2018) 495–520.
- [27] L. Prandtl, 7. bericht über untersuchungen zur ausgebildeten turbulenz,  
 855 *Z. Angew. Math. Mech.* 5 (1925) 136–139.
- [28] A. A. R. Townsend, *The Structure of Turbulent Shear Flow*, 2nd ed., Cam-  
 bridge University Press, 1976.
- [29] I. Marusic, J. P. Monty, Attached eddy model of wall turbulence, *Annu.*  
*Rev. Fluid Mech.* 51 (2019) 49–74.
- 860 [30] S. B. Pope, *Turbulent Flows*, Cambridge University Press, 2000.
- [31] Rakhi, M. Klein, J. A. Medina M., H. Schmidt, One-dimensional turbulence  
 modelling of incompressible temporally developing turbulent boundary lay-  
 ers with comparison to DNS, *J. Turbul.* 20 (2019) 506–543.
- [32] I. Marusic, B. J. McKeon, P. A. Monkewitz, H. M. Nagib, A. J. Smits,  
 865 K. R. Sreenivasan, Wall-bounded turbulent flows at high Reynolds num-  
 bers: recent advances and key issues, *Phys. Fluids* 22 (2010) 065103.
- [33] M. Lee, R. D. Moser, Direct numerical simulation of turbulent channel flow  
 up to  $Re_\tau \approx 5200$ , *J. Fluid Mech.* 774 (2015) 395–415.
- [34] R. D. Moser, J. Kim, N. N. Mansour, Direct numerical simulation of  
 870 turbulent channel flow up to  $Re_\tau \approx 590$ , *Phys. Fluids* 11 (1999) 943–945.

- [35] H. Abe, R. A. Antonia, Relationship between the heat transfer law and the scalar dissipation function in a turbulent channel flow, *J. Fluid Mech.* 830 (2017) 300–325.
- [36] D. A. Shaw, T. J. Hanratty, Turbulent mass transfer rates to a wall for large Schmidt numbers, *AIChE J.* 23 (1977) 28–37.
- [37] A. Z. Owinoh, J. C. R. Hunt, A. Orr, P. Clark, R. Klein, H. J. S. Fernando, F. T. M. Nieuwstadt, Effects of changing surface heat flux on atmospheric boundary-layer flow over flat terrain, *Boundary-Layer Meteorol.* 116 (2005) 331–361.
- [38] B. A. Kader, Temperature and concentration profiles in fully turbulent boundary layers, *Int. J. Heat Mass Transfer* 24 (1981) 1541–1544.
- [39] H. Kawamura, H. Abe, Y. Matsuo, DNS of turbulent heat transfer in channel flow with respect to Reynolds and Prandtl number effects, *Int. J. Heat Fluid Flow* 20 (1999) 196–207.
- [40] B. A. Kader, A. M. Yaglom, Heat and mass transfer laws for fully turbulent wall flows, *Int. J. Heat Mass Transfer* 15 (1972) 2329–2351.
- [41] T. Wei, P. Fife, J. Klewicki, P. McMurtry, Scaling heat transfer in fully developed turbulent channel flow, *Int. J. Heat Mass Transfer* 48 (2005) 5284–5296.
- [42] H. Kawamura, K. Ohsaka, H. Abe, K. Yamamoto, DNS of turbulent heat transfer in channel flow with low to medium-high Prandtl number fluid, *Int. J. Heat Fluid Flow* 19 (1998) 482–491.
- [43] I. Kolesnichenko, P. Frick, V. Eltishchev, S. Mandrykin, F. Stefani, Evolution of a strong electrovortex flow in a cylindrical cell, *Phys. Rev. Fluids* 5 (2020) 123703.
- [44] C. A. Sleicher, M. W. Rouse, A convenient correlation for heat transfer to constant and variable property fluids in turbulent pipe flow, *Int. J. Heat Mass Transfer* 18 (1975) 677–683.

- [45] M. van Reeuwijk, K. S. Lari, Asymptotic solutions for turbulent mass  
900 transfer at high Schmidt number, *Proc. R. Soc. A* 468 (2012) 1676–1695.
- [46] F. W. Dittus, L. M. K. Boelter, Heat transfer in automobile radiators of  
the tubular type, *Int. Comm. Heat Mass Transfer* 12 (1985) 3–22.
- [47] W. H. McAdams, *Heat Transmission*, McGraw-Hill Series in Chemical En-  
gineering, 3rd ed., McGraw-Hill, New York, 1954.
- 905 [48] W. M. Kays, M. E. Crawford, *Convective Heat and Mass Transfer*,  
McGraw-Hill Series in Mechanical Engineering, 2nd ed., McGraw-Hill, New  
York, 1980.
- [49] S. Tschisgale, T. Kempe, Deterioration of heat transfer in turbulent channel  
flows due to nanoparticles, *Int. J. Heat Mass Transfer* 175 (2021) 121392.